Robotic Inspection of Underground Utilities for Construction Survey Using a Ground Penetrating Radar

Jinglun Feng[1]; Liang Yang, Ph.D.[2]; Ejup Hoxha[3]; Biao Jiang[4]; and Jizhong Xiao[5]

Abstract: Ground penetrating radar (GPR) is a very useful nondestructive evaluation (NDE) device for locating and mapping underground assets prior to digging and trenching efforts in construction. This paper presents a novel robotic system to automate the GPR data-collection process, localize underground utilities, and interpret and reconstruct the underground objects for better visualization, allowing regular non-professional users to understand the survey results. This system is composed of three modules: (1) an omnidirectional robotic data-collection platform that carries a RGB-D camera with inertial measurement unit (IMU) and a GPR antenna to perform automatic GPR data collection and tag each GPR measurement with visual positioning information at every sampling step, (2) a learning-based migration module to interpret the raw GPR B-scan image into a two-dimensional (2D) cross-section model of objects, and (3) a three-dimensional (3D) reconstruction module, i.e., 30.0% GPRNet, to generate underground utility model represented as fine 3D point cloud. Comparative studies were performed on synthetic data and field GPR raw data with various incompleteness and noise. Experimental results demonstrated that our proposed method achieves a higher GPR imaging accuracy in mean intersection over union (IoU) than the conventional back-projection (BP) migration approach, and 6.9% − 7.2% less loss in Chamfer distance (CD) than point cloud model reconstruction baseline methods. The GPR-based robotic inspection provides an effective tool for civil engineers to detect and survey underground utilities before construction. **DOI: 10.1061/(ASCE)CP.1943-5487.0001062.**

Introduction

Ground penetrating radar (GPR) is widely used in nondestructive testing (NDT) for civil engineers to locate and map buried objects (e.g., utilities, rebars, underground storage tanks, and metallic or plastic conduits), measure pavement thickness and properties, and locate and characterize subsurface features (e.g., subgrade voids below concrete slabs or behind retaining walls). The GPR inspection is a wave-propagation technique that transmits a pulse of polarized high-frequency electromagnetic (EM) waves into the subsurface media. An EM wave attenuates as it travels in media and reflects when it encounters a material change. A GPR antenna would thus record the strength and traveled time of each reflected pulse (Demirci et al. 2012b). The reflections are then amplified, processed, and displayed on a screen as an A-scan signal, analogous to a waveform in an oscilloscope. When the GPR device moves along a straight line perpendicular to utility pipes, the ensemble of the A-scans forms a B-scan, which is shown as the hyperbolic feature, indicating the objects' locations as well (Li et al. 2016a; Yuan et al. 2018a).

There are two pain-points limiting the GPR applications on revealing subsurface flaws and helping underground object reconstruction. The first one is how to determine GPR's position and orientation accurately and in real time, and synchronize with GPR measurements at each GPR sampling step. In current practice of GPR data collection, inspectors would either move a GPR cart (Li et al. 2016b) along premarked grid lines and count on the survey wheel encoder to trigger GPR measurements while obtaining the accurate linear positions for detailed mapping and survey, or count on a high-precision global positioning system (GPS) to provide accurate position information for detecting large underground objects or surveying a large area along nonlinear trajectories.

In encoder-triggered manual data collection, it is time-consuming and tedious for the inspector to premark the grid intersection points, take notes and photographs, and push the GPR device to closely follow the gird lines in *X-Y* directions. On the other hand, GPS equipment is expensive and its accuracy is still not sufficient for the three-dimensional (3D) GPR imaging projects where every scan must be accurately localized and targets must be resolved in inches. In addition, GPS accuracy is degraded in urban environments where buildings may obstruct and distort GPS signals (Wells et al. 1987). Furthermore, GPS cannot work in indoor environments.

The second challenge is how to develop an efficient 3D GPR imaging method to visualize the subsurface objects allowing regular nonprofessional people to understand. Unfortunately, the current commercial GPR postprocessing software cannot process GPR data collected from nonlinear trajectories.

To address these challenges, we implement a low-cost vision-based positioning method, tag the pose information at each GPR sample, and develop GPR analysis software that provides a holistic solution for automated GPR data collection and 3D GPR imaging and reconstruction.

As shown in Fig. 1, the main contributions of this work can be summarized as follows:

[1]Ph.D. Candidate, Dept. of Electrical and Engineering, City College of New York, 160 Convent Ave., New York, NY 10031. ORCID: https://orcid.org/0000-0002-2416-7150. Email: jfeng1@ccny.cuny.edu

[2]Research Assistant, Dept. of Electrical and Engineering, City College of New York, 160 Convent Ave., New York, NY 10031. Email: lyang1@ccny.cuny.edu

[3]Ph.D. Candidate, Dept. of Electrical and Engineering, City College of New York, 160 Convent Ave., New York, NY 10031. ORCID: https://orcid.org/0000-0003-2658-3411. Email: ehoxha@ccny.cuny.edu

[4]Assistant Professor, Dept. of Natural Sciences, Hostos Community College, 500 Grand Concourse, Bronx, New York, NY 10451. Email: bjiang@hostos.cuny.edu

[5]Professor, Dept. of Electrical and Engineering, City College of New York, 160 Convent Ave., New York, NY 10031 (corresponding author). Email: jxiao@ccny.cuny.edu

Note. This manuscript was submitted on April 29, 2022; approved on August 10, 2022; published online on October 12, 2022. Discussion period open until March 12, 2023; separate discussions must be submitted for individual papers. This paper is part of the ***Journal of Computing in Civil Engineering***, © ASCE, ISSN 0887-3801.

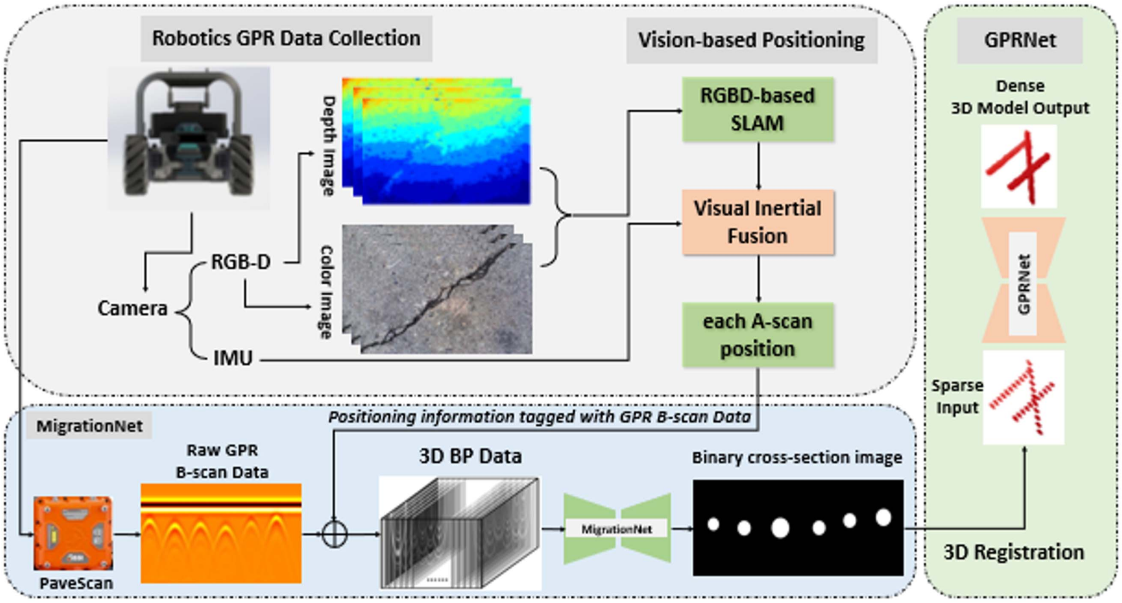

Fig. 1. System architecture.

- An omnidirectional robot is developed that carries a GPR antenna on the chassis, moves forward, backward, and sideways in a fast and swift manner and enables the detailed survey to be conducted in arbitrary nonlinear trajectories. Compared with Feng et al. (2022), this robot is more portable and lightweight and can run with a consistent and stable trajectory.
- A learning-based module that uses two separate deep neural networks (DNNs) is presented. The first network aims to interpret the B-scan data and the second network reveals the object model structure based on the interpreted data and presents the 3D model in point cloud.
- Compared with Feng et al. (2021a), we further augmented our GPR data set with the point cloud models. We released this unique data set to contribute to the learning-based GPR processing communities (Feng 2022).

Fig. 1 shows the system archictecture, where the system contains three modules. First, a vision-based robotic GPR data-collection module automates the GPR data collection and tags the GPR data with visual positioning information. Second, MigrationNet interprets the B-scan image to a two-dimensional (2D) cross-section image of the object model. Third, GPRNet registers 2D cross-section images into the 3D space as a sparse model and transfers the sparse model to the 3D dense model of subsurface objects.

This paper is organized as follows. In the section "Related Works," we review related works on conventional GPR migration methods, as well as the recent GPR 3D reconstruction algorithms. Section "Vision-Aided Robotic GPR Data Collection" introduces the robotic GPR data-collection system and verifies the vision-based positioning accuracy. Sections "MigrationNet for GPR Data Interpretation" and "GPRNet: GPR Pipes Reconstruction Network for 3D Modeling" present the learning-based GPR data processing methods. Section "Experimental Study" introduces the proposed GPR data set and presents extensive experimental results. At last, section "Conclusion" concludes the paper and presents future research directions.

Related Works

GPR migration and model reconstruction are popular topics in NDT and civil engineering and have been extensively investigated in the last 2 decades.

Conventional GPR Migration Methods

GPR migration is a process that converts the unfocused raw B-scan radargram data into a focused target. Conventional migration methods can be roughly categorized into Kirchhoff migration (Schneider 1978), the phase-shift migration (Gazdag 1978), the finite-difference method (Claerbout and Doherty 1972), and back-projection (BP) algorithm.

The BP algorithm is the most significant and commonly used 2D imaging reconstruction method in the GPR industry (Demirci et al. 2012a, b). When GPR emits the radiation pulse, the BP algorithm assumes this wave path shares a semisphere pattern with an equal energy level. After GPR receives the radiation pulse back, the BP algorithm stack the radiation energy along the hyperbolic trajectory; then, the sum of the responded amplitude could reflect the target region (Schofield et al. 2020; González-Huici et al. 2014; Feng et al. 2022).

To further improve the effectiveness of the conventional BP algorithm, several modified BP methods have been proposed. Xie et al. (2020) presented the bifrequency BP (BBP) to enhance the visualization quality of the subsurface objects, especially for grouting. Fast BP (FBP) was proposed by Zhou et al. (2011); it is an approximation method that could run faster by simplifying the computation of subsurface dielectric (Gharamohammadi et al. 2019). In addition, many researchers focused on the cross-correlation BP (CBP) method (Cai et al. 2020; Lin et al. 2020; Jacobsen and Birkelund 2010; Zhang et al. 2015). CBP can cut down the round trip time-of-flight from a stimulating source to a focal point and back to a receiver. Moreover, Liu et al. (2020) improved the BP algorithm by integrating a correction factor for radiation pattern in the subsurface to reduce the negative influence of the traditional homogeneous radiation pattern on GPR. Filtered BP (FBP) is another modified BP method. Schofield et al. (2020) and Chetih and Messali (2015) investigated this method to get rid of the noise effects back in the GPR images.

Three-Dimensional GPR Imaging Methods

In recent years, research on GPR imaging has made commendable progress in academia (Dinh et al. 2021; Hou et al. 2021; Qin et al. 2021; Xiang et al. 2021). Researchers at Texas A&M University published a series of papers on automatic subsurface pipeline mapping and 3D reconstruction using a GPR and a camera (Li et al. 2019; Chou et al. 2016, 2017, 2018; Li et al. 2018; Chou et al. 2020). They modeled the GPR sensing process and proved the hyperbola response for general scanning with nonperpendicular angles, which is novel. They fused visual-simultaneous localization and mapping (V-SLAM) and encoder readings with GPR scans to classify hyperbolas into different pipeline groups and applied the J-linkage and maximum likelihood method to estimate the radii and locations of all pipelines. However, the average error for pipe radius estimation was over 35%, which is not good enough for practical use (Li et al. 2019). They encountered calibration and synchronization problems and had to use customized artificial landmarks to synchronize camera poses (temporally evenly spaced) to the GPR data (spatially evenly spaced) (Chou et al. 2020).

Similarly, researchers at the University of Vermont published several papers related to 3D reconstruction from both ground and air-coupled multistatic GPR (Pereira et al. 2018b, 2019a, b, 2020). The main contribution of these works was the consideration of phase compensation for different receiver antennas. They not only stacked the B-scan images to model the 3D multistatic GPR imaging, but also took the different gains and dielectric contrast of each receiver antenna into consideration and further fused it with a Hessian-based enhancement filter to formulate the final 3D reconstruction model. However, the noise reconstructed in the 3D model was still not clearly removed by the proposed method, which makes the 3D model not good enough for visualization. In addition, a Google Tango device was used to provide position information to GPR scan data (Pereira et al. 2018a). However, the limitation of this method is that Google Tango is no longer in service and thus this method cannot be implemented in practice.

Vision-Aided Robotic GPR Data Collection

Robotic Data-Collection Platform

As shown in Fig. 2, we developed an omnidirectional robot for the inspection of underground utilities. Our robot has four Mecanum wheels that allow forward, backward, and sideways motion to follow grid pattern without spinning. A PaveScan GPR antenna from Geophysical Survey System Inc. (GSSI) (Nashua, New Hampshire) was installed at the bottom of the robot chassis to perform GPR data collection. An Intel Realsense (Santa Clara, California) RGB-D camera (D435i) was mounted at the robot's front. This camera could support indoor and outdoor working environment, which boosts the robustness for our vision-based positioning system. A six-axis inertial measurement unit (IMU) was embedded in the camera to provide accurate and robust pose estimation. The robot carried a rechargeable battery and a high-level controller (i.e., Intel NUC) to provide power to the system and synchronize the pose data with GPR scan data.

Fig. 2. Omnidirectional robot for vision-based GPR data collection, where a GPR antenna is installed at the bottom of the robot chassis. (Images by authors.)

Fig. 3 depicts the inverse kinematics model of the omnidirectional robot. The highly maneuverable design allows the robot to move in any direction without spinning and thus provides free motion trajectories for the GPR data collection. The robot motion satisfies the following equation:

$$
\begin{aligned}
v_x &= \frac{R}{4}(w_1 + w_2 + w_3 + w_4)\\
v_y &= \frac{R}{4}(-w_1 + w_2 - w_3 + w_4)\\
\omega_o &= \frac{R}{4(L_2 \tan\alpha + L_1)}(-w_1 + w_2 + w_3 - w_4)
\end{aligned}
\tag{1}
$$

where R = radius of the Mecanum wheel; $\{w_i\}_{i=1}^{N=4}$ = angular velocity of each Mecanum wheel; L_1 and L_2 = width and length of the robot chassis, respectively; α = angle of the roller, which equals 45°; v_x, v_y, and ω_o = linear velocity in x- and y-directions and the angular velocity of the robot chassis, respectively; $\{x_i\}_{i=1}^{N=4}$ and $\{y_i\}_{i=1}^{N=4}$ = local coordinate frame of each Mecanum wheel; x and y = robot coordinate frame of the robot motion; and o = center of the robot chassis and the robot coordinate origin.

Eq. (2) demonstrates how robot position and orientation update. In detail, the current pose $(x_{t+1}, y_{t+1}, \theta_{t+1})$ is updated according to its pose information (x_t, y_t, θ_t) at the previous time, as well as the robot orientation angle θ and unit sampling time Δt

$$
\begin{aligned}
\theta_{t+1} &= \theta_t + \omega_o \times \Delta t\\
x_{t+1} &= x_t + v_x \cos\theta_{t+1} \times \Delta t - v_y \sin\theta_{t+1} \times \Delta t\\
y_{t+1} &= y_t + v_x \sin\theta_{t+1} \times \Delta t + v_y \cos\theta_{t+1} \times \Delta t
\end{aligned}
\tag{2}
$$

To remotely control the robot motion and conduct GPR data collection, we designed an Android application (APP) whose graphic user interface (GUI) is illustrated in Fig. 4. We provided

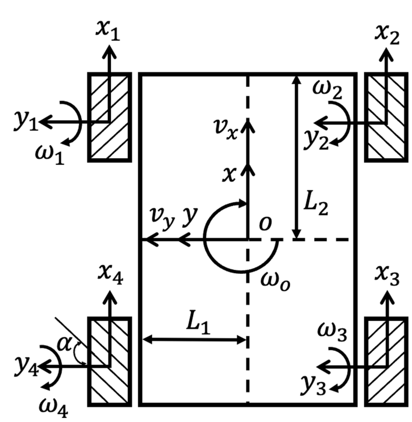

Fig. 3. Structural schematic diagram of our GPR cart.

J. Comput. Civ. Eng., 2023, 37(1): 04022049

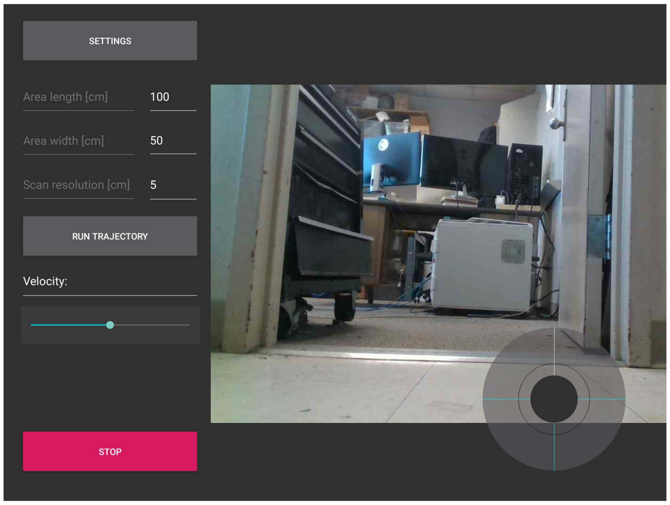

Fig. 4. Remote-controller APP GUI of our robot data-collection platform showing FPV.

two control modes in this remote-control APP: (1) automatic; and (2) manual. In automatic mode, the user needs to define the width, length, and grid resolution of the survey area; then, our APP will generate a zigzag path along the grid to cover the survey area according to the predefined parameters, and the robot starts the data collection automatically. The user could stop an automatic data collection by pressing the red stop button at the bottom left of the GUI.

On the other hand, manual mode can be activated anytime to control the robot with the virtual joystick button (the double circles at the bottom right of the GUI). The virtual joystick button controls the robot motion direction by pushing the middle gray circle to the desired angle. If the joystick is released and the gray circle rests in the middle, then the robot stops. Moreover, the user could define the linear velocity of the robot through the sliding bar and show the first person view (FPV) of the robot in the window.

Tagging GPR Measurement with Pose Information

It is very crucial that the GPR data are tagged with the robot pose at each GPR sampling, which will eliminate the constraint of needing GPR data collection along straight lines in X-Y directions. Allowing the robot to scan in arbitrary and irregular trajectories makes the GPR data collection much easier and facilitates the 3D GPR imaging data analysis.

Specifically, our robot carries a RGB-D camera embedded with an IMU sensor to collect RGB and depth images of the construction surface, together with the corresponding IMU data, e.g., quaternion, angular velocity, and linear velocity. Then, by taking advantage of the ORB-SLAM3 (Campos et al. 2021) algorithm, it takes RGB images and depth images as the input to conduct visual odometry and fuses with IMU measurement to perform real-time localization. Then, we implemented a time synchronizer function in Robot Operation System (ROS), which takes in messages of different types from multiple sources and outputs them only if it has received a message on each of those sources with the same timestamp. It is used to synchronize the GPR sampling with vision-based positioning data so that the GPR data collection would not be constrained to a straight line.

The frame rate of the RGB-D camera is 30 Hz, and the IMU update rate is 200 MHz. Through interpolation, we achieved 200 Hz for position updates. Because the PaveScan GPR sampling rate is 100 Hz, we synchronized the vision-based positioning and GPR updating at 100 Hz in the experiments. In other words, our robotic data-collection system could collect 100 scan data tagged with pose data per second, and the spacing between the consecutive measurements would be 5 mm when robot moves with a 0.5 m/s linear velocity. It demonstrates that the vision-based accurate positioning solution has met the low latency requirement because 100–200 Hz is more than good enough for almost all commercial GPR applications. Fig. 5 illustrates an example of how GPR B-scan data are collected and tagged with pose information in a zigzag motion as well as a spiral motion, and it does not require the intervention of the human inspector.

Furthermore, we conducted an accuracy test of the robot motion using a VICON system (Hauppauge, New York) (Merriaux et al. 2017). As shown in Fig. 6, we controled the robot move in a zigzag pattern, where lines indicates the ground truth of the motion trajectory provided by the VICON system, and the r motion trajectory estimated by an RGB-D camera. Fig. 7 and Eq. (3) denote the root square error (RSE) between the ground truth and vision-based trajectory. The mean RSE is around 1 cm, which satisfies the requirement for highly accurate positioning by the GPR industry

$$\text{Mean RSE} = \sqrt{\frac{\sum_{i=1}^{N} \left\| y(i) - \hat{y}(i) \right\|^2}{N}} \tag{3}$$

where N = number of position samples; i = ith position sample; and $y(i)$ and $\hat{y}(i)$ = ground-truth position and estimated position, respectively.

MigrationNet for GPR Data Interpretation

We present the learning-based GPR data processing methods as shown in Fig. 8, which consists of MigrationNet and GPRNet, as well as a point cloud conversion process. In this section, we train a network, MigrationNet, to interpret the input B-scan data to a cross-section image of the underground object model.

Given the kth B-scan data $\mathcal{B}^k = \{(\mathcal{A}_i^k, \mathbf{T}_i)\}_{i=1}^N \in \mathbb{R}^{N\times M\times 1}$ where $k = 1, \ldots, K$, we assume $\mathcal{B}^k$ consists of N tuples of A-scans $\mathcal{A}_i^k = \{(\mathbf{a}_j, \mathbf{t}_j)\}_{j=1}^M \in \mathbb{R}^{M\times 1}$ along with their corresponding pose $\mathbf{T}_i \in \mathbb{R}^{3\times 4}$ (where in $\mathcal{A}_i^k$, M indicates the number of samples in an A-scan data; $\mathbf{a}_j$ and $\mathbf{t}_j$ denote the amplitude and traveling time of the jth A-scan sample). Our goal is to distill B-scan data into a BP-based representation Θ. In addition, we are interested in the GPR data processing Θ that allows us to interpret the $\Theta(\mathcal{B})$ into a clear, user-friendly cross-section image of the underground object model. In the following, we first formalize Θ and then discuss the details of interpretation algorithm in Φ. In all, Algorithm 1 describes the processing of this approach, which is called MigrationNet (Feng et al. 2021b).

Algorithm 1. MigrationNet for GPR data interpretation

Input:

B-scan data $\mathcal{B}^k = \{(\mathcal{A}_i^k, \mathbf{T}_i)\}_{i=1}^N \in \mathbb{R}^{N\times M\times 1}$;

Output:

A cross-section image $\mathcal{I}^k$ of the subsurface utility's geometry;

for $k \leftarrow 1, n$ **do**
  Downsample the B-scan data $\mathcal{B}^k$ to $\hat{\mathcal{B}}^k$
  Sparse back-project $\hat{\mathcal{B}}^k$ via function Θ to get the input $\mathbf{Z}^k$.
  Extract $\{\mathbf{f}_i\}_{i=1}^{N=3} \in \mathbb{R}^{M\times N\times 512}$ from $\{\mathcal{E}_i^M\}_{i=1}^{N=3}$;
  Estimate $\mathcal{I}^k$ through the decoder.
end for
return $\Phi(\mathbf{Z}^k) = \mathcal{I}^k$;

J. Comput. Civ. Eng., 2023, 37(1): 04022049

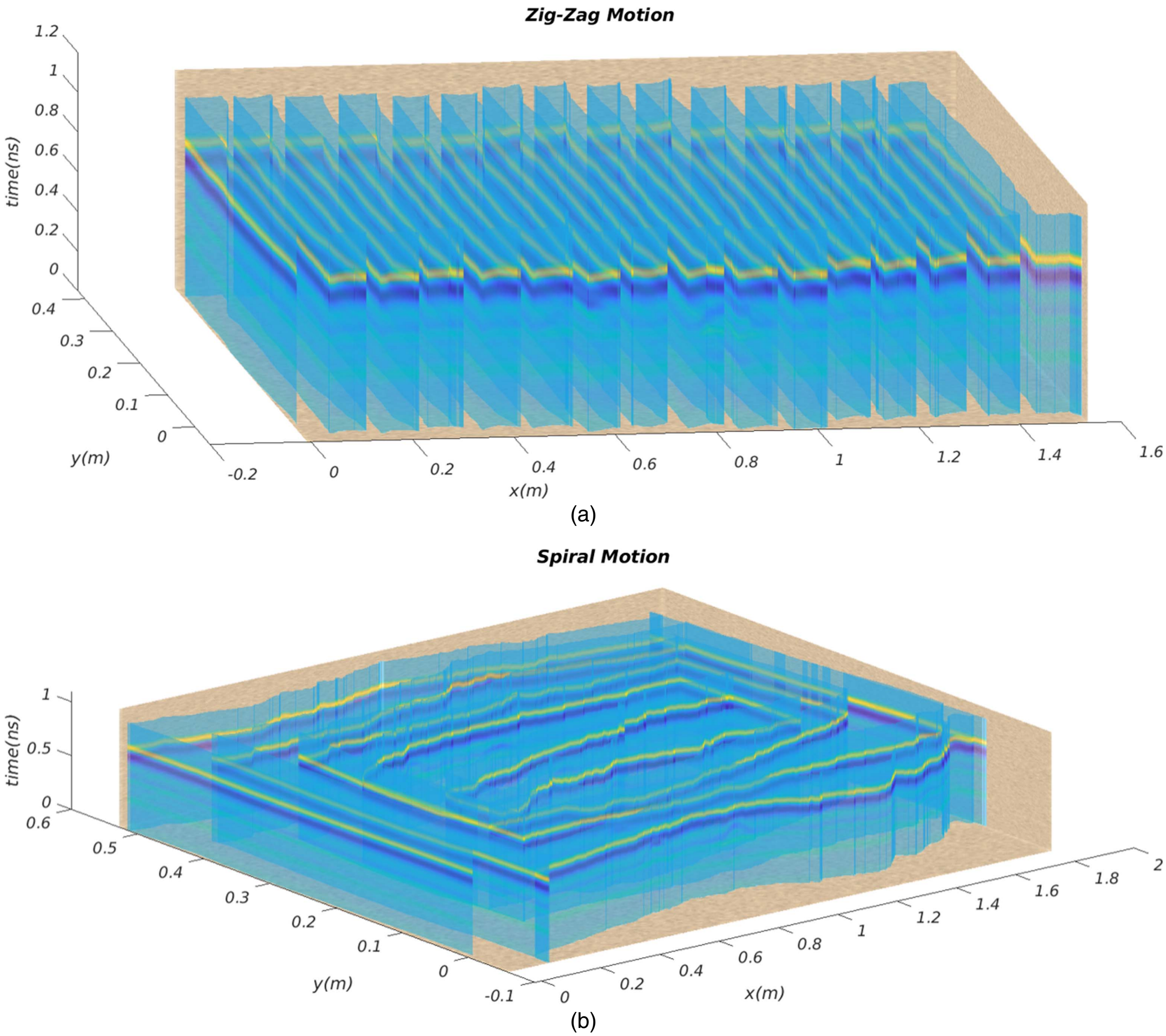

Fig. 5. B-scan profile tagged with metric positioning information when a robot moves along a zigzag and spiral trajectory: (a) B-scan profile in a zigzag motion trajectory; and (b) B-scan profile in a spiral motion route.

Sparse Back-Projection Aggregation

As discussed in section "Related Works," the BP approach Θ serves as a common solution to process the GPR data (Li et al. 2019). However, there are some limitations existing in the BP approach. First of all, it needs to back-project each A-scan $\mathcal{A}_i^k$ into a predefined 3D volumetric map. Second, each A-scan $\mathcal{A}_i^k$ covers a cone-volume of subsurface, and it usually overlaps with other neighbor A-scans. The back-projection of each A-scan would result in heavy computation during the fusion because of the indexing, which is computation expensive and requires large memory to support the computation.

In order to address this challenge, we introduce a multispatial-resolution algorithm to aggregate the A-scans, where the resolution denotes how many A-scan measurements $\hat{N}$ $(0 < \hat{N} < N)$ from a $\mathcal{B}^k$ are used for back-projection. In particular, because each $\mathcal{B}^k$ might have a different number of A-scan measurements N, for any $\mathcal{B}^k$ whose number of A-scan measurements are less than 1,024, we only picked $\hat{N} = 256$, 128, and 64 A-scan measurements for back-projection and stack them in the spatial domain as the input. This is how we distinguish the different spatial resolutions in the input data. Otherwise, for those $\mathcal{B}^k$ with more than 1,024 A-scan measurements, we introduced a sliding-window crop operation to split the B-scan data into multiple segments. As introduced in Eq. (4), we fixed the sliding window length to 1,024, where q is equal to the ceiling value of this equation, which represents the number of cropped B-scans after the trim operation

$$q = \lfloor N/1024 \rfloor \tag{4}$$

Then, by taking advantage of the BP algorithm, each sample's amplitude in an A-scan is converted into a semisphere shape at its corresponding traveling time. As illustrated in Fig. 9, the brighter semisphere indicates the higher-amplitude part in the A-scan. Furthermore, the radius of each semisphere in a BP image indicates the depth between the ground and the object, which is illustrated by Eq. (5) (Li et al. 2019)

$$\forall\ \mathcal{A}_i^k \in \hat{\mathcal{B}}^k, \qquad (x - \mathbf{t}_x)^2 + (y - \mathbf{t}_y)^2 = (\mathbf{a}_j * \mathbf{t}_j)^2$$
$$y < 0, 1 < i < N, 1 < j < M \tag{5}$$

where $\mathbf{t}_x$ and $\mathbf{t}_y$ = position of the current A-scan $\mathcal{A}_i^k$.

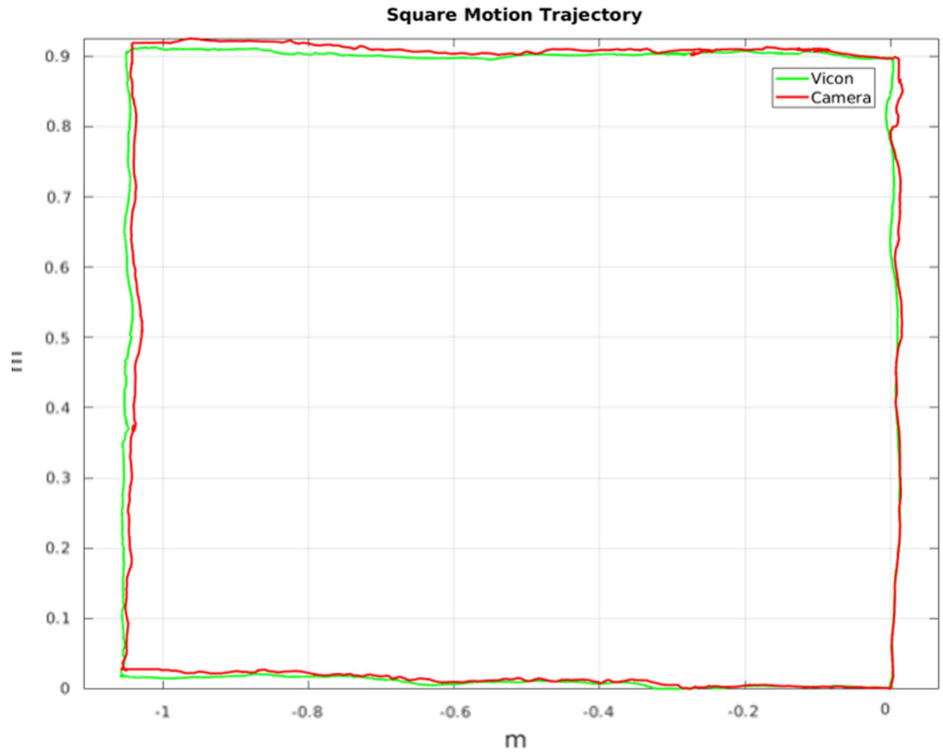

Fig. 6. Motion trajectory between ground truth, which is provided by a VICON system, and camera. This motion is in a 2×2-m square pattern.

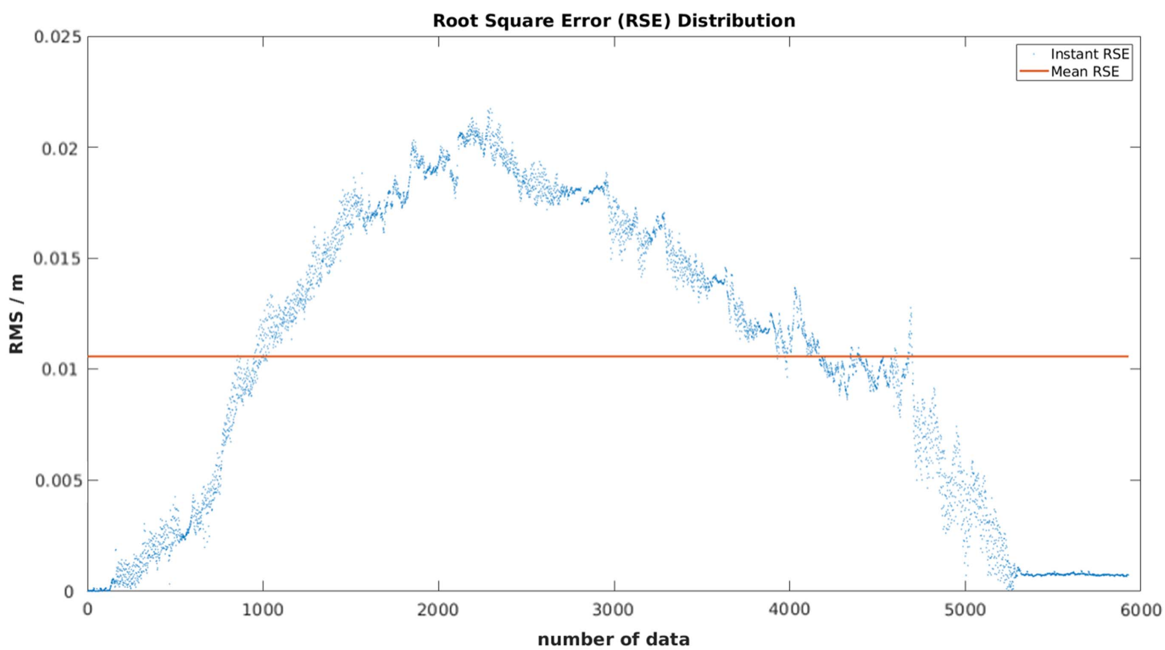

Fig. 7. RSE error distribution between the ground-truth motion and estimated motion provided by visual positioning. The mean RSE error is only 1.03 cm, which could meet the positioning accuracy in practical GPR collection.

In particular, given a 2D back-projected data $\mathcal{P}_i^k$ converted from $\mathcal{A}_i^k$ as shown in Fig. 9, its height and width are the same as a raw B-scan $\mathcal{B}^k$, which are equal to M and N, respectively. It is because BP is an algorithm that aggregates each back-projected data $\mathcal{P}_i^k$ from a B-scan $\mathcal{B}^k$, and the intersection part in the aggregated BP data $\sum_{i-1}^{N} \mathcal{P}_i^k$with the highest energy level indicates a potential target.

In summary, we leverage on the BP principle to represent and process the cropped B-scan $\hat{\mathcal{B}}^k$ as a function Θ

$$\Theta{:}\mathbb{R}^{\hat{N}\times M\times 1} \rightarrow \mathbb{R}^{\hat{N}\times M\times N}, \qquad \hat{\mathcal{B}}^k \mapsto \Theta(\hat{\mathcal{B}}^k) = \sum_{i=1}^{\hat{N}} \mathcal{P}_i^k = \mathbf{Z}^k \quad (6)$$

In this way, a sparse-stacked multiresolution input $\mathbf{Z}^k$ is created. We chose to sparsely aggregate the back-projected data $\mathcal{P}_i^k$ because

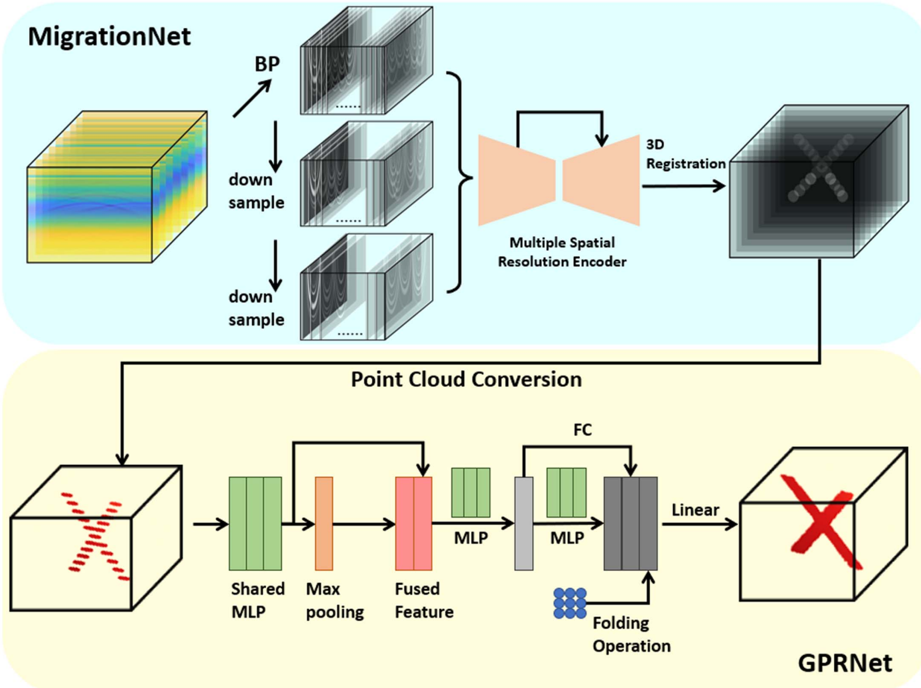

Fig. 8. Network architecture. MigrationNet aggregates the BP data with multiple resolutions and interprets those BP data into a set of 2D images that indicate the cross section of the subsurface utilities. Then, the cross-section images are converted into the sparse point cloud and GPRNet completes the sparse point cloud to make it dense and continuous.

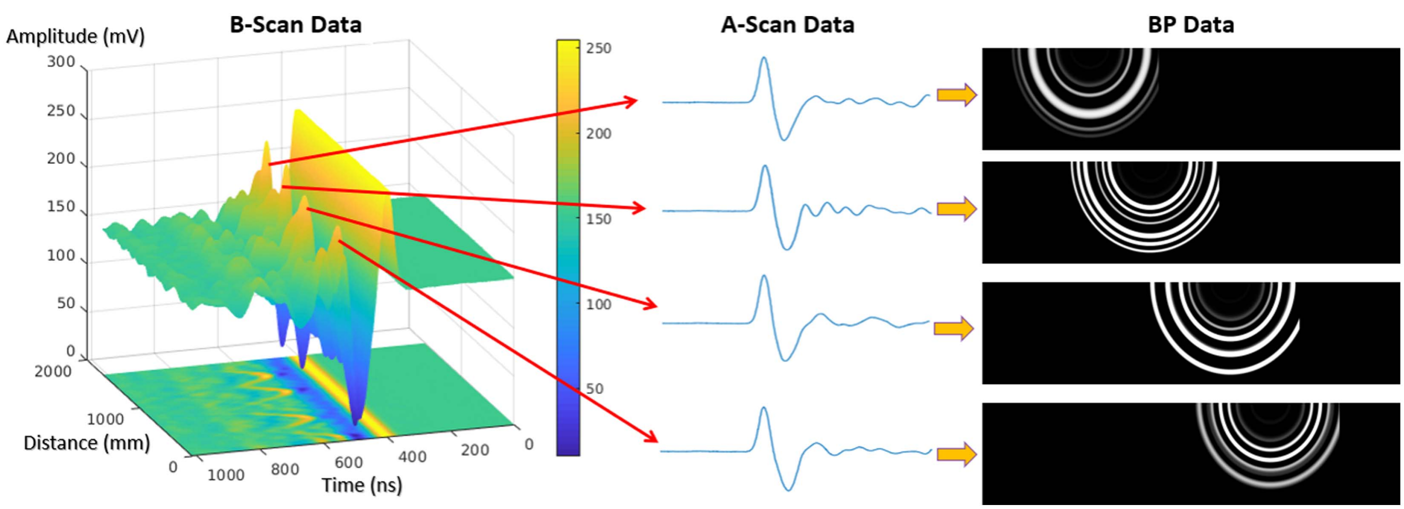

Fig. 9. Given a B-scan data combined with A-scan, the BP algorithm converts the A-scan raw data into a set of semispheres.

a sparse data can decrease the computational cost and can provide multiple resolution of the input data in the spatial domain. We provide more details and experiments in section "Experimental Study."

MigrationNet Formulation

Given a sparse-stacked input $\mathbf{Z}^k$, we introduce a interpretation algorithm Φ that maps a sparse-stacked B-scan data to an image $\mathcal{I}^k$ as follows:

$$\Phi{:}\mathbb{R}^{\hat{N}\times M\times N} \to \mathbb{R}^{M\times N\times 1}, \qquad \Theta(\hat{\mathcal{B}}^k) \mapsto \Phi(\mathbf{Z}^k) = \mathcal{I}^k \tag{7}$$

In particular, Φ is composed of an encoder, which has multiple spatial resolutions to extract features from multiple resolution input $\mathbf{Z}^k$, and a decoder, to interpret the features and predict a cross-section image $\mathcal{I}^k$ of the subsurface utility's geometry.

Multiple Spatial Resolution Encoder

A multiresolution representation is the key for Φ to interpret $\mathbf{Z}^k$. Thus, we first introduce our feature extractor, named Multiple Spatial Resolution Encoder (MSRE). Here, we take inspiration from the Feature Pyramid Network (FPN) (Lin et al. 2017) structure. FPN belongs to the class of object detection algorithms that inhereted the feature capture ability by introducing a multiresolution input and reveal the rich local structure information in the spatial domain.

Specifically, the input $\mathbf{Z}^k \in \mathbb{R}^{\hat{N}\times M\times N}$ has three resolutions, where $\hat{N} = \{256, 128, 64\}$. Thus, to extract features from $\mathbf{Z}^k$, we use three independent feature extractors $\{\mathcal{E}_i^M\}_{i=1}^{N=3}$ composed of several downsampling groups $\{\mathbf{d}_i\}_{i=1}^{N=3}$. Each downsampling group $\{\mathbf{d}_i\}_{i=1}^{N=3}$ is a combination of two convolution layers and one max-pooling layer, where the kernel size $\{s_i^k\}_{i=1}^{N=3}$ of the max-pooling layer is different. Specifically, when $\hat{N} = 256$, the kernel size of the max-pooling layer in the corresponding extractor is equal to $s_1^k = 8$. In addition, the kernel size in the max-pooling layer is set to $s_2^k = 4$ when $\hat{N} = 128$, whereas the max-pooling kernel size is equal to $s_3^k = 2$ when $\hat{N} = 64$. Hence, three corresponding latent feature maps $\{\mathbf{f}_i\}_{i=1}^{N=3} \in \mathbb{R}^{M\times N\times 512}$ are extracted from $\{\mathcal{E}_i^M\}_{i=1}^{N=3}$.

Decoder

To estimate a cross-section image $\mathcal{I}^k$ from the extracted features, here we introduce the decoder frame work. Given our current feature maps $\{\mathbf{f}_i\}_{i=1}^{N=3} \in \mathbb{R}^{M\times N\times 512}$, we concatenate them to $\mathbf{F} \in \mathbb{R}^{M\times N\times 1536}$ and pass them through the encoder. In particular, this decoder is composed of four upsampling groups $\{\mathbf{u}_i\}_{i=1}^{N=4}$, and each group contains two convolutional layers and one deconvolutional layer. Besides, we also take advantage of skip connections, which skip-connects features between $\{\mathbf{d}_i\}_{i=1}^{N=3}$ and $\{\mathbf{u}_i\}_{i=1}^{N=4}$.

To summarize, the decoder interprets the concatenated feature map $\mathbf{F}^M \in \mathbb{R}^{M\times N\times 1536}$ to a cross-section binary image $\mathcal{I}^k \in \mathbb{R}^{M\times N\times 1}$, where the open region indicates the cross-section of the utilities and the solid area indicates the background.

Loss Design and Training

To constrain the shape and size of the underground cylindrical objects, we leverage on a joint loss $\mathcal{L}$ that consists of two terms: a structure similarity loss and a cross entropy loss.

In particular, in most of the real nondestructive testing test cases, objects such as rebars, utilities, and PVC pipes all have a round shape cross section. Hence, it is necessary to compare structure similarity between the predicted image and the ground truth to maintain the proper size and shape. Inspired by Wang et al. (2004), Zhao et al. (2015), and Godard et al. (2017), we demonstrate the structure comparison loss between predicted image X and ground truth Y as follows:

$$\mathcal{L}_S = \frac{\sigma_{xy} + C}{\sigma_x\sigma_y + C} \tag{8}$$

where σ_x and σ_y = standard deviation as an estimate of the image contrast; C = constant value; and σ_{xy} = covariance, which is calculated as follows:

$$\sigma_{xy} = \frac{1}{M\times N - 1}\sum_{q=1}^{M\times N}(x_q - \mu_x)(y_q - \mu_y) \tag{9}$$

where μ_x and μ_y = mean intensity of the predicted image $\mathcal{I}^k$ and ground truth, respectively; x_q and y_q = each pixel's coordinate; and $M\times N$ =number of pixels in the image.

We then use cross entropy loss (Ronneberger et al. 2015) as the second loss expression in this joint loss design

$$\mathcal{L}_{\mathrm{CE}} = \sum_{x_k\in\mathcal{M}} w^l(x)\log(p(x_{k,l})) \tag{10}$$

where x_k = element in given input; M, $p(x_{k,l})$ = element x_k probabilistic prediction over class l; and w^l = weight of each classes.

Finally, our loss function is expressed in Eq. (11), where λ_i and λ_j denote the weight of cross entropy loss and structure loss that satisfy the relation as $\lambda_i + \lambda_j = 1$

$$\mathcal{L} = \lambda_i\mathcal{L}_S + \lambda_j\mathcal{L}_{\mathrm{CE}} \tag{11}$$

For training, the weights governing the terms in loss function was set to $\lambda_i = 0.1$ and $\lambda_j = 0.9$. We also used the stochastic gradient descent (SGD) and selected momentum as 0.9 and weight decay as 1×10^{-8}. As for the initial learning rate (LR) and input scale, by evaluating the average accuracy, average precision, average recall as well as F1 score in training data set with different LR and scale, the learning rate was set to 5×10^{-6} and the input scale was 0.25.

GPRNET: GPR Pipes Reconstruction Network For 3D Modeling

In this section, we introduce Algorithm 2 which is a 3D modeling network that reconstructs underground pipes (named as GPRNet).

Algorithm 2. GPR-based subsurface pipe reconstruction
Input:
The interpreted cross-section image, $\mathcal{I}^k \in \mathbb{R}^{M\times N\times 1}$;
The pose associated with B-scan data, $\mathbf{T}^k$;
Output:
Dense point cloud set $\mathbf{P^D}$ of the subsurface pipes;
1: **for** $k\leftarrow 1, n$ **do**
2: Convert the given $\mathcal{I}^k$ and its corresponding pose $\mathbf{T}^k$ to a sparse point cloud set $\mathbf{P}$.
3: **end for**
4: Extract the point feature vector $\{\mathbf{v}_i\}_{i=1}^{N=3}$ from $\{\mathcal{E}_i^G\}_{i=1}^{N=3}$;
5: Estimate $\mathbf{P^D}$ through the decoder.
6: **return** $\Psi(\mathbf{P}) = \mathbf{P^D}$;

From 2D Image to 3D Point Cloud

We introduced the GPR interpretation algorithm in last section, and we now expect to reveal the spatial information of the subsurface objects' structure based on the interpretation results. Hence, we first register the predicted binary cross-section image set $\mathcal{I} = \{\mathcal{I}^k \in \mathbb{R}^{M\times N\times 1} | k = 1, 2, \ldots, K\}$ into the 3D space according to its pose $\mathbf{T}$, where $\mathbf{T} = \{\mathbf{T}^k = \{\mathbf{T}_i\}_{i=1}^{N} | k = 1, 2, \ldots, K\}$ and k represents the kth image/pose corresponding to B-scan data $\mathcal{B}^k$. The pose $\mathbf{T}_i$ was obtained from the vision-based positioning introduced in section "Vision-aided Robotic GPR Data Collection." In this way, we can make sure for any interpreted image $\mathcal{I}^k$, it shares the same pose information $\mathbf{T}^k$ as its corresponding B-scan data $\mathcal{B}^k$.

We further convert the registered image set to get a sparse point cloud set $\mathbf{P} = \{p_i\}_{i=1}^{C}$. We regard this point cloud $\mathbf{P}$ as consisting of C points with each point $p_i \in \mathbb{R}^3$.

Specifically, $\mathcal{I}^k$ is a binary image, and the white pixel value is equal to 1. Thus, we register these 2D white pixels into a 3D space by aggregating multiple images, and the third dimension is provided by visual positioning information that tagged with the image.

Once obtain $\mathbf{P}$, we use iterative farthest point sampling (IFPS), which is a sampling strategy applied in Pointnet++ (Qi et al. 2017b) to get a set of skeleton points. IFPS can represent the distribution of the entire point sets better compared with random sampling, and it is more efficient than convolutional neural networks (CNNs) (Huang et al. 2020). After the implementation of IFPS, we evenly distribute each point cloud $\mathbf{P} = \{p_i\}_{i=1}^{C}$ as input to GPRNet, where C equals 1,500.

GPRNet Formulation

Formally, given a set of sparse point cloud $\mathbf{P} = \{p_i\}_{i=1}^{C}$, GPRNet aims to complete the gap between sparse point clouds and predict a continuous, dense point cloud representation $\mathbf{P^D} = \{p_i^d\}_{i=1}^{C'}$, where $p_i^d \in \mathbb{R}^3$ and $C' > C$. We now reason about this procedure through Ψ, and Ψ defines a learning model that has an encoder decoder structure. This procedure is illustrated in the following:

$$\Psi:\mathbb{R}^{C\times 3} \rightarrow \mathbb{R}^{C'\times 3}, \qquad \mathbf{P} \mapsto \Psi(\mathbf{P}) = \mathbf{P^D} \tag{12}$$

Encoder

Similar to our MigrationNet, GPRNet's encoder $\{\mathcal{E}_i^G\}_{i=1}^{N=3}$ takes advantage of multiresolution structure. Each subnet $\mathcal{E}_i^G$ is a PointNet layer (Qi et al. 2017a) that consists of three convolutional multilayer perceptron (MLP) layers and one max-pooling layer. Given the input point cloud set $\mathbf{P}$, each subnet $\mathcal{E}_i^G$ extracts the point feature vector $\{\mathbf{v}_i\}_{i=1}^{N=3} \in \mathbb{R}^{C\times j}$, where $j = \{256{,}128, 64\}$, respectively.

Then, a max-pooling layer is conducted on each $\{\mathbf{v}_i\}_{i=1}^{N=3}$ to obtain three intermediate features $\{\mathbf{g}_i\}_{i=1}^{N=3}$ with the same dimension as $\{\mathbf{v}_i\}_{i=1}^{N=3}$. Furthermore, we concatenate each point feature vector $\{\mathbf{v}_i\}_{i=1}^{N=3}$ and each intermediate feature $\{\mathbf{g}_i\}_{i=1}^{N=3}$ together and express as a fused feature matrix. At last, another MLP layer extracts the feature map as a $\mathbf{F}^G \in \mathbb{R}^{C\times 896}$, which is represented in light gray color, as shown in Fig. 8.

Hierarchical Scene Representation

Our key idea is to represent the point cloud geometry and appearance with hierarchical feature layers and incorporate the inductive biases of decoders at different spatial resolutions. The fully connected decoder (Achlioptas et al. 2018) is good at predicting the global geometry of point cloud but ignores the local features. In contrast, the FoldingNet decoder (Yang et al. 2018) is good at generating a smooth local feature. Hence, we take advantage of these decoders and introduce a decoder with a hierarchical structure similar to that of Huang et al. (2020), which contains the fully connected (FC) layer, MLP layer, and FoldingNet layer. In particular, $\mathbf{F}^G$ is passed through an FC layer as well as an MLP layer, and concatenate together as $\mathbb{F} \in \mathbb{R}^{896\times 3}$. In addition, we leverage the folding operation, where a patch of nine points is generated at each xyz map in the feature $\mathbb{F}$. Thus, we can obtain the detailed output consisting of 896×9 (8,064) points. That is to say, a dense point cloud output, $\mathbf{P^D}$, is thus generated from our multiresolution decoder via the fully-connected and folding operations. $\mathbf{P^D} = \{p_i^d\}_{i=1}^{C'}$, C' is equal to 8,064.

Loss Design and Training

To constrain and compare the difference between the predicted point cloud set $\mathbf{P^D}$ and the ground-truth point cloud set $\mathbf{P^{GT}}$, an ideal loss must be differentiable concerning point locations and invariant to the permutation of the point cloud. In this paper, we use Chamfer distance (CD) (Fan et al. 2017) loss $\mathcal{L}_{\mathrm{CD}}$ to calculate the average closest point distance between $\mathbf{P^D}$ and $\mathbf{P^{GT}}$, which is shown in Eq. (13)

$$\mathcal{L}_{\mathrm{CD}} = \frac{1}{\mathbf{P^D}} \sum_{p_m \in \mathbf{P^D}} \min_{p_n \in \mathbf{P^{GT}}} \|p_m - p_n\|_2 + \frac{1}{\mathbf{P^{GT}}} \sum_{p_n \in \mathbf{P^{GT}}} \min_{p_m \in \mathbf{P^D}} \|p_n - p_m\|_2 \tag{13}$$

where p_m and p_n = point in $\mathbf{P^D}$ and $\mathbf{P^{GT}}$, respectively.

The Chamfer distance finds the nearest neighbor in the ground-truth point set. Thus, it can force output point clouds to lie close to the ground truth and be piecewise smooth.

Experimental Study

In this section, we first introduce the preparation of the field and synthetic GPR data used for training and testing. Then, we present several experiments such as a comparison study and ablation study to demonstrate the effectiveness of our proposed learning-based method.

Data Preparation

To verify the proposed DNN models in this paper, we prepared a GPR B-scan data set for training and testing purposes. The data set we provide contains both synthetic and field B-scan data.

Field GPR Data Generation

We firstly collect the field GPR data with our robotics GPR inspection system on a concrete slab at City College of New York (CCNY) Robotics Lab Testing Pit. As mentioned in section "Vision-aided Robotic GPR Data Collection," the GPR sensor we used is a GSSI PaveScan RDM 1.0, with a 2-GHz frequency and 20-cm max depth detection range. Fig. 10 shows the design and layout of concrete slab, whose dimension is $2.84 \times 1.11 \times 0.22$ m (length $\times$ width $\times$ thickness), and there are 10 pipes embedded in the concrete slab with different sizes, depths, and materials. Notably, the two gray pipes are PVC pipes, where their dimensions are 7.62 cm; the leftmost PVC pipe is also filled with electrical wires. Moreover, there are three normal PVC pipes, where the diameters are 3.175 cm. In addition, there are three other normal

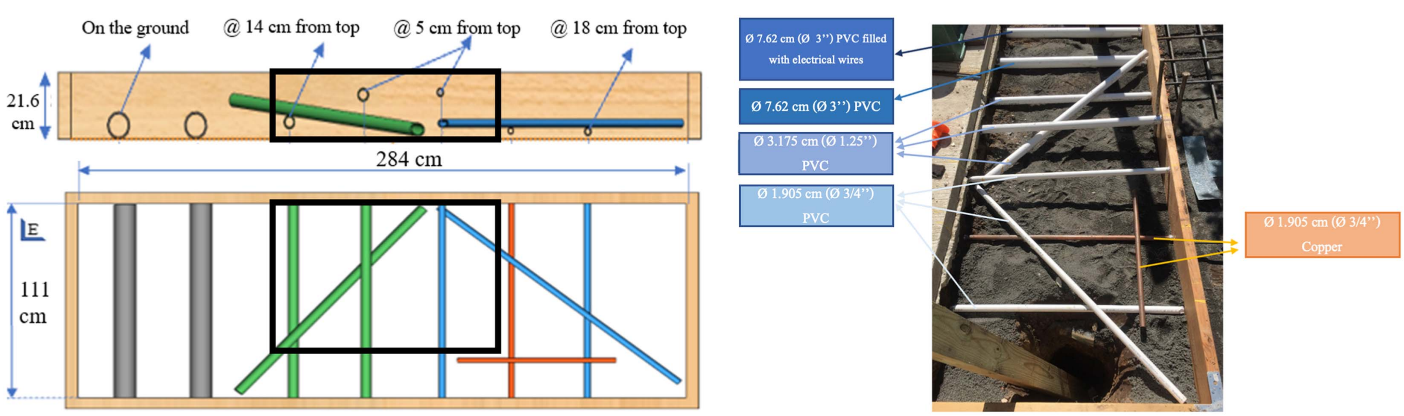

Fig. 10. Design details and ground truth of the concrete slab buried with pipes with different locations, dimensions, and directions.

PVC pipes with a smaller dimensions of 1.905 cm. Finally, there are two copper pipes with dimensions of 1.905 cm.

We controled the omnidirectional robot to move along a zigzag path to scan the slab. In the end, there were 24 automated GPR tests conducted, which contributed 120 field B-scan data to our data set.

gprMax Data Generation

However, the collected field data is still not enough for the DNN model training purpose. Thus, by taking advantage of gprMax (Warren et al. 2016), we built a synthetic testing environment that simulates the real NDT condition. Most common assetst buried underground are cylindrical with a round cross section, for example, rebars, utilities, and PVC pipes. Our simulated environment emulated this condition and involved cylindrical objects with different locations, dimensions, and directions. Furthermore, in order to match the data collection in field GPR test, we also used a synthetic GPR antenna with 2-GHz frequency (Stadler and Igel 2018; Warren and Giannopoulos 2011; Giannakis et al. 2018). At last, we made the spacing of consecutive measurements to 5 mm to match the same property in our field data collection.

Specifically, we built 507 different synthetic concrete slabs with 4,563 B-scan data in gprMax. The simulated GPR pulse was a Gaussian norm wave that had a central frequency $f_c = 2$ GHz. The distance between transmitter and receiver of the antenna was set to 5 cm, with a sensing time window of 5 ns. The surrounding medium of all the concrete slab models was set to a similar value that could mimic the concrete environment, where the relative permittivity was equal to 7 and conductivity was set to 0.01. Assuming the nonmagnetic property of the surrounding environment, the relative permeability was set to 1. All the simulated objects were designed as a perfect electric conductor (PEC). At last, we made the spacing of consecutive measurements to 5 mm to match with the same property in our field data collection. All the slabs have the same dimension, which is $0.35 \times 0.25 \times 0.25$ m (length $\times$ width $\times$ thickness). There were two to six PEC circular-section reinforcing bars buired in each slab with different radii, directions, and depths. The aforementioned properties make our generalized B-scan data set have a similar configuration compared with the real GPR data. The front view figure of our synthetic slabs is shown in Fig. 11.

In all, we have combined 4,683 synthetic and real B-scan data in this article, and we used 3,510 B-scan data in training, 723 data in validation, and 450 B-scan data for testing.

Ground Truth of Point Cloud Model Generation

Due to the well-designed field and synthetic slab, we were able to easily generate the ground-truth point cloud for training purpose. In particular, because we know the physical properties, layout, and dimension of each pipe, we can simply calculate the linear equation based on that information. Then, for each point along a line, we adopted a cross-section region within a circle or ellipse. Specially, if an utility pipe is parallel with the x- or y-direction, then the adopted region is a circle and the radius of this circle r_c is equal to pipe's radius r; otherwise, if the pipe is diagonal inserted in a slab with a slope s, the cross-section region will be an ellipse, and its semiminor axis length r_b is equal to pipe's radius r abd the semimajor axis length r_a is equal to $a \times \arctan s$.

All points were normalized to have zero-mean per axis and unit-variance. Following prior convention, we generated 8,096 points in each ground-truth point cloud set during both training and testing.

Experiments Study of MigrationNet

Effectiveness of MigrationNet

Fig. 12(a) shows the collected onsite GPR B-scan data, which areillustrated in a highlighted hotmap format. Figs. 12(b and d) represent the back-projected data in the time domain and are displayed with a highlighted parula color code; specifically, Fig. 12(b) shows the conventional migration result using a sparse input BP data, and Fig. 12(d) uses the full BP data as input. We further applied the Hilbert transform filter in Fig. 12(d). The filtered BP image is shown in Fig. 12(f) with a highlighted parula color code. Fig. 12(e) indicates the ground truth of the cross-section image corresponding to the field B-scan data, and Fig. 12(c) demonstrates the B-scan interpretation result using MigrationNet.

The quantitative effectiveness comparison between the conventional migration and MigrationNet is presented in Table 1. In the conventional migration method, the energy level is continuous distributed from 0 to 1. In contrast, the energy level in MigrationNet is binary distributed. That is, 0 stands for the background, and 1 presents the target area. For this reason, we convert the conventional migration results to the binary image by selecting the luminance threshold as 0.45. This luminance threshold would convert the region where the energy level is greater than 0.45 to 1, and the rest of the region to 0. In this way, we can compare the GPR image reconstruction results between the conventional and learning-based methods with multiple metrics.

In particular, we used multiple metrics for the quantitative evaluation. The metrics shown in Eqs. (14)–(18) include mean intersection over union (IoU), pixel accuracy, mean square error (MSE), signal-to-noise ratio [SNR (dB)], and structural similarity index (SSMI). For metrics mean IoU, pixel accuracy, SSMI, and MSE, the larger the value, the better the performance it stands for; in contrast, for SNR, the lower the value, the better performance it stands for. As indicated in Table 1, compared with the conventional migration method, MigrationNet gains a 30% higher performance in mean IoU, 5.7% higher performance in pixel accuracy, 24.3% higher performance in MSE, 22.2% higher performance in SSMI, and 42.5% less noise in SNR. We can conclude that MigrationNet could effectively improve the performance of GPR imaging reconstruction

$$\mathrm{IoU}(S_t, S) = \frac{S_t \cap S}{S_t \cup S} = \frac{S_t \cap S}{|S_t| + |S| - S_t \cap S} \tag{14}$$

$$\text{Pixel accuracy} = \frac{\mathrm{TP} + \mathrm{TN}}{\mathrm{TP} + \mathrm{TN} + \mathrm{FP} + \mathrm{FN}} \tag{15}$$

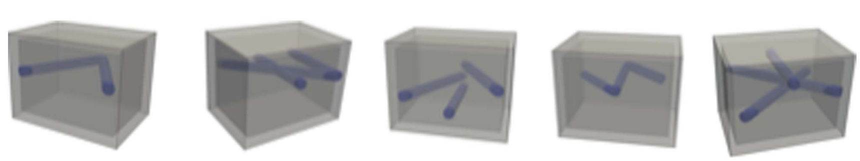

Fig. 11. CAD models built by gprMax. All the models emulate the concrete slab property where multiple pipes with different sizes, directions, and depths are inserted.

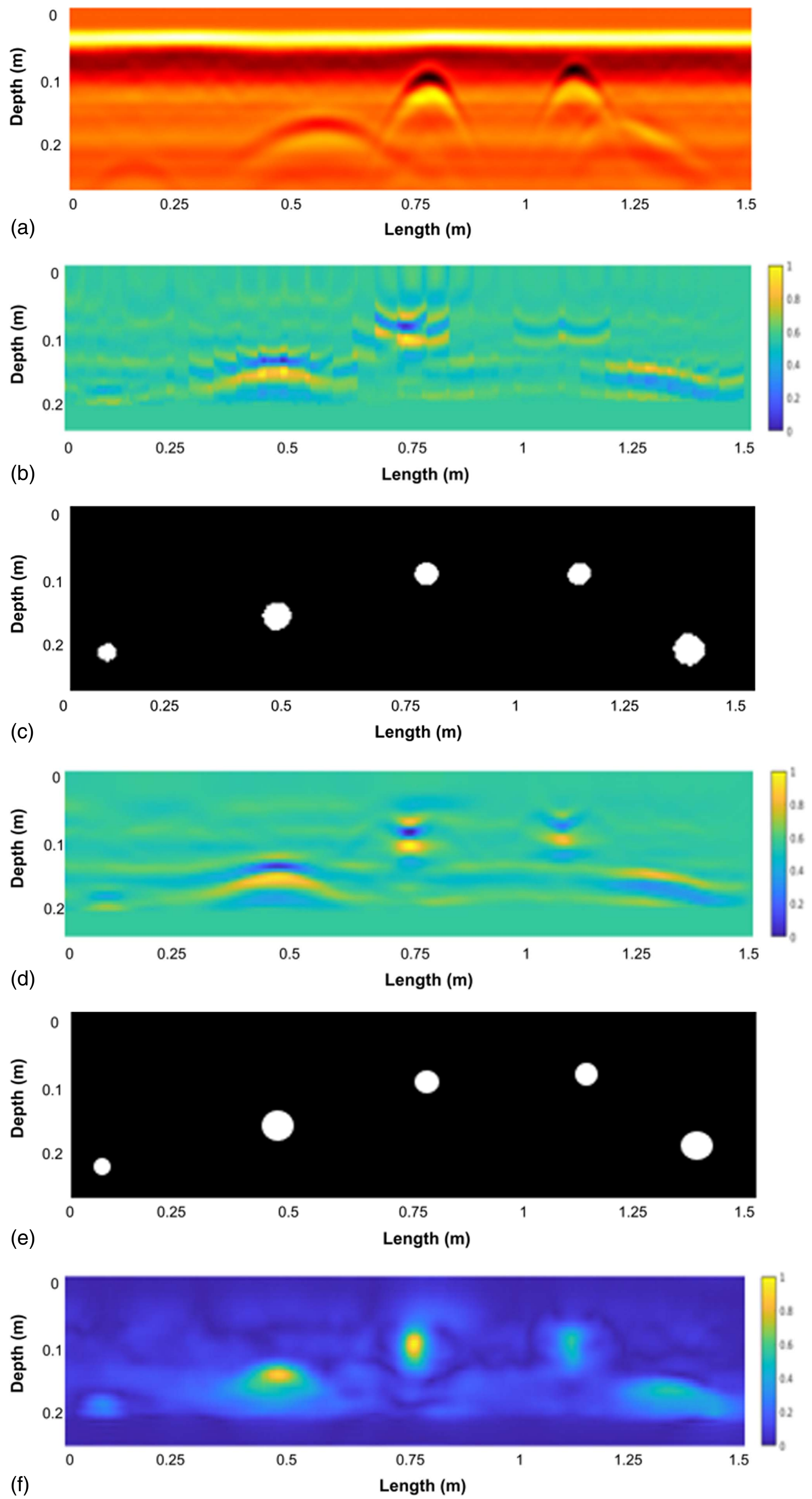

Fig. 12. Qualitative migration result comparison between MigrationNet and conventional migration method: (a) raw real GPR B-scan image; (b) sparse BP image aggregated in the time domain; (c) predicted image regarding plot (a); (d) full BP image aggregated in the time domain (e) ground-truth image regarding plot (a); and (f) filtered BP image using Hilbert transform algorithm.

Table 1. Quantitative results on MigrationNet: Migration effectiveness comparison between conventional migration and MigrationNet

Metrics	Conventional migration	MigrationNet
Mean IoU	62.99	**89.97**
Pixel accuracy (%)	90.48	**95.70**
MSE	531.71	**661.13**
SSMI	0.770	**0.941**
SNR (dB)	5.747	**3.307**

Note: Bold values indicate the better results.

$$\mathrm{MSE} = \frac{1}{n}\sum_{i=1,j=1}^{n}(X_{i,j} - Y_{i,j})^2 \tag{16}$$

$$\mathrm{SNR} = 10 \times (\log 10(X/Y)) \tag{17}$$

$$\mathrm{SSIM}(X,Y) = \frac{(2\mu_X\mu_Y + C_1)(2\sigma_{XY} + C_2)}{(\mu_X^2 + \mu_Y^2 + C_1)(\sigma_X^2 + \sigma_Y^2 + C_2)} \tag{18}$$

where S_t = ground-truth region of interests (ROI); S = predicted ROI; TP, TN, FP, and FN = true positive, true negative, false positive, and false negative of the pixel label, respectively; i, j = pixel index in image X and image Y; in Eq. (17), X = noise signal and is compared with respect to ground-truth image Y; μ_X, μ_Y, σ_X, σ_Y, and σ_{XY} = local means, standard deviations, and cross-covariance for images X, Y; and C_1 and C_2 = constant values.

We then provide the noise robustness test of MigrationNet. To do this, we added Gaussian white noise, salt and pepper noise, and speckle noise, respectively, to the input GPR data. Each type of the noise has four different variance and noise density parameters, which are 0.05, 0.1, 0.2, and 0.5. We finally compared the root-mean square error (RMSE) metric for the conventional migration method and MigrationNet. As illustrated in Table 2 and Fig. 13, we could find that our proposed method has high noise robustness. In contrast, the noise would significantly degrade the migration results when deploying the conventional method.

At last, we compared the average processing time between the BP-based migration inference time and the MigrationNet inference time. The result is given in Table 3, which indicates that MigrationNet outperformed the BP-based migration method in computation cost due to its sparse-input assumption.

Ablation Study for MigrationNet

Why Does B-Scan Sampling Density Matter?. It is interesting to discuss the relationship between the channel numbers of input stacked BP data and the migration performance. In common sense, a small spacing between consecutive measurements would lead to a high-performance migration result (i.e., a sharper, brighter, and more focused target point in the energy map). Still, it also brings a costly computation problem when processing a large amount of data. Therefore, how to balance the measurement sampling density and migration result is worth investigating.

Given raw B-scan data, we extracted BP data with different numbers of channels, such as 64, 128, 256, $128 + 64$, and $256 + 128$, as indicated in Table 4. In this way, we can distinguish the GPR imaging performances among all input types. Specifically, the metrics we used for performance evaluation were MSE, SNR (dB) and SSMI. The lower the MSE value, the better performance it presents, whereas the higher SSMI and SNR values, the better performance they present.

The results indicate that our current input resolution of $256 + 128 + 64$ gained the best performance on SNR, and second best performance on MSE and SSMI compared with other resolutions of input data. When the input channel number decreases to 64, it will go beyond the MigrationNet's ability to learn spatial features from such a sparse input. We also chose to reserve the raw input data without doing any sampling process, which leds to the best performance, but with more computation and longer processing time as expected.

Why Does the Structure Similarity Loss Matter?. To verify the effectiveness of our joint loss, we further provided a comparison study with or without structural similarity loss, as demonstrated in Table 5. As indicated in Table 5, our joint loss has a better performance than the single cross-entropy loss, which reveals that this hybrid loss design can help capture structure information with a clearer boundary.

Experimental Study of GPRNet

Effectiveness of GPRNet

To evaluate the effectiveness of GPRNet, we compared it with baseline methods such as PCN (Yuan et al. 2018b) and TopNet (Tchapmi et al. 2019) as indicated in Table 6 and Fig. 14. In particular, we used three evaluation metrics for the quantitative effectiveness comparison in Table 6: CD, earth mover's distance (EMD) (Achlioptas et al. 2018), and $\mathcal{L}_1$ distance. CD indicates the average squared distance between two points; EMD represents the average distance between corresponding points; $\mathcal{L}_1$ denotes the average distance from each point cloud to the centroid point in a point cloud set. Table 6 indicates that our proposed method outperforms other methods in all the three evaluation metrics. Compared with the PCN and TopNet, GPRNet gains 5.9% less and 7.2% less Chamfer distance respectively. We upscaled all the metrics by 10^3 for better perception.

In addition, the qualitative comparison result among GPRNet, PCN, and TopNet is depicted in Fig. 14. Compared with PCN and TopNet, our proposed method obtains a better qualitative performance on different model structures where utility pipes have different radii embedded with different angles, depths, and positions. Moreover, GPRNet can present the fine details of the object structure, such as a pipe with a joint at the center as shown in Fig. 14. Based on the quantitative and qualitative results, we can conclude that our method outperforms the other methods in spatial continuity and shape accuracy level.

Table 2. Noise robustness comparison: RMSE comparison between conventional migration and MigrationNet

	Conventional migration			MigrationNet		
Metrics	Gaussian	Salt and pepper	Speckle	Gaussian	Salt and pepper	Speckle
Without noise		37.3491			3.3500	
Variance and noise density = 0.05	54.3589	51.6030	56.1675	11.4624	11.2508	10.2708
Variance and noise density = 0.1	62.2094	61.1385	61.8539	17.8093	16.3628	16.0731
Variance and noise density = 0.2	75.3084	77.7894	76.1743	32.1583	30.9074	29.5939
Variance and noise density = 0.5	92.4765	90.1059	92.0384	45.3853	42.8437	41.2759

J. Comput. Civ. Eng., 2023, 37(1): 04022049

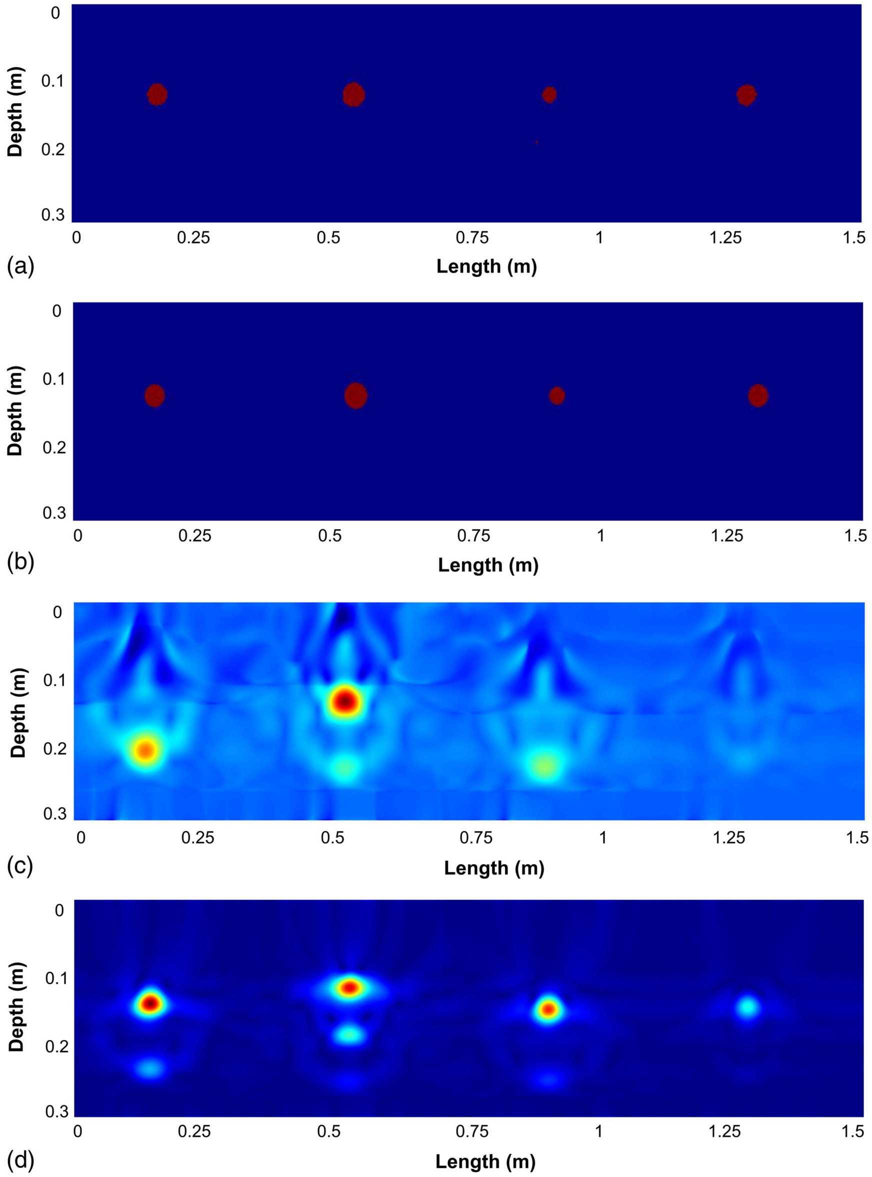

Fig. 13. Qualitative noise robustness comparison between conventional and proposed migration method with/without salt and pepper noised input: (a) GPR 2D image interpretation results with salt and pepper noise using MigrationNet; (b) GPR 2D image interpretation results without salt and pepper noise using MigrationNet; (c) conventional migration results with salt and pepper noise; and (d) conventional migration results without salt and pepper noise.

Table 3. Computational cost comparison between BP-based migration and MigrationNet

Method	Average time cost (ms)
BP-based migration	23.12
MigrationNet	**5.68**

Note: Bold values indicate the better results.

Furthermore, we analyzed the effectiveness of our network with different sampling numbers in input point clouds, where the number N varied among 1,000, 1,500, 2,000, 3,000, and 4,000. In Table 7, we notice that the performance of GPRNet increases when the input number of point clouds increases. That is to say, the more point clouds sampled in the input, the less complicated the reconstruction task is. This experiment enlightens us to balance the sampling number of input point clouds and the performance of the reconstruction point cloud model. Thus, we decided to use

Table 4. Evaluation performance comparison with different spatial resolution inputs of MigrationNet on three metrics

Multiresolution input channels	MSE	SSMI	SNR (dB)
256 + 128 + 64	661.1313	0.9413	**3.3066**
256 + 128	717.1609	0.9250	3.5947
128 + 64	832.5777	0.9199	5.7474
256	1.4553×10^3	0.9035	7.1199
128	1.433×10^3	0.9075	7.0553
64	—	—	—
Raw input	**630.7042**	**0.9565**	3.3849

Note: Bold values indicate the better results.

1,500 as the number of sparse input point cloud in all other studies because it requires less collected B-scan data and computation time, but it is still can achieve a relatively good reconstruction performance.

Table 5. Performance comparison between the joint loss and cross entropy loss in MigrationNet

Metrics	Joint loss	Cross entropy loss
Mean IoU	**89.97**	87.65
Pixel accuracy (%)	**95.70**	94.65
E_distance	**35.5809**	38.9276
MSE	**661.1313**	764.5629
SSMI	**0.9413**	0.9378
SNR (dB)	**3.3066**	5.0584

Note: Bold values indicate the better results.

Table 6. Quantitative effectiveness comparison results between GPRNet and other baselines

Metrics	GPRNet	PCN	TopNet
CD	**6.328**	6.725	6.821
EMD	**6.536**	6.827	7.173
$\mathcal{L}_1$	**2.016**	2.430	2.621

Note: Bold values indicate the better results.

In addition, the average cost of inference time between our method and the baseline methods was determined. We calculated the inference time on every test data on our data set for each method and then obtained the average time cost. As presented in Table 8, TopNet gains the best time computation performance over the others. That is because both GPRNet and PCN have a multiresolution structure decoder, which increases the computational cost.

Noise Robustness of GPRNet

To evaluate the effectiveness of our method under different sensor noise levels, we perturbed the input sparse point cloud with multiple Gaussian white noise levels as shown in Fig. 15, where the noise variances are 0.01, 0.05, 0.1, and 0.2, respectively. We further

Table 7. Evaluation performance comparison with various numbers of input point cloud

Sampling number of input point cloud	CD	EMD	$\mathcal{L}_1$
1,000	7.264	7.498	2.629
1,500	6.328	6.536	2.016
2,000	6.174	6.236	1.823
3,000	5.524	5.563	1.585
4,000	4.773	4.925	1.430

Note: Bold values indicate the better results.

performed a quantitative study on noise comparisons among GPRNet, PCN, and TopNet with different metrics of CD, EMD, and $\mathcal{L}_1$ distance as illustrated in Table 9. We could conclude our proposed method gains higher robustness against noise in comparison with PCN and TopNet.

Field Test Model Reconstruction Comparison

This section compares the effectiveness of the 3D reconstruction model between the proposed GPRNet and conventional migration method with the field data collected on the CCNY testbed. As illustrated in Fig. 16, the solid outlined window region in Fig. 16(a) indicates the data-collection area and the three 2D images demonstrate migration results from the top view. The pipe in Fig. 16(a) could not be recovered; the reason is that its depth was out of the GPR detection range (Fig. 10 shows the concrete slab details). Furthermore, we also illustrated the raw and filtered 3D models generated by conventional migration methods in Fig. 16(b), where the deployed filter is Hessian filter (Pereira et al. 2020). Due to the limitation of the conventional migration method, the noise data are hard to be cleaned out and differentiated from the raw GPR data, which causes the filtered 3D model to still be hard to recognize by normal GPR users.

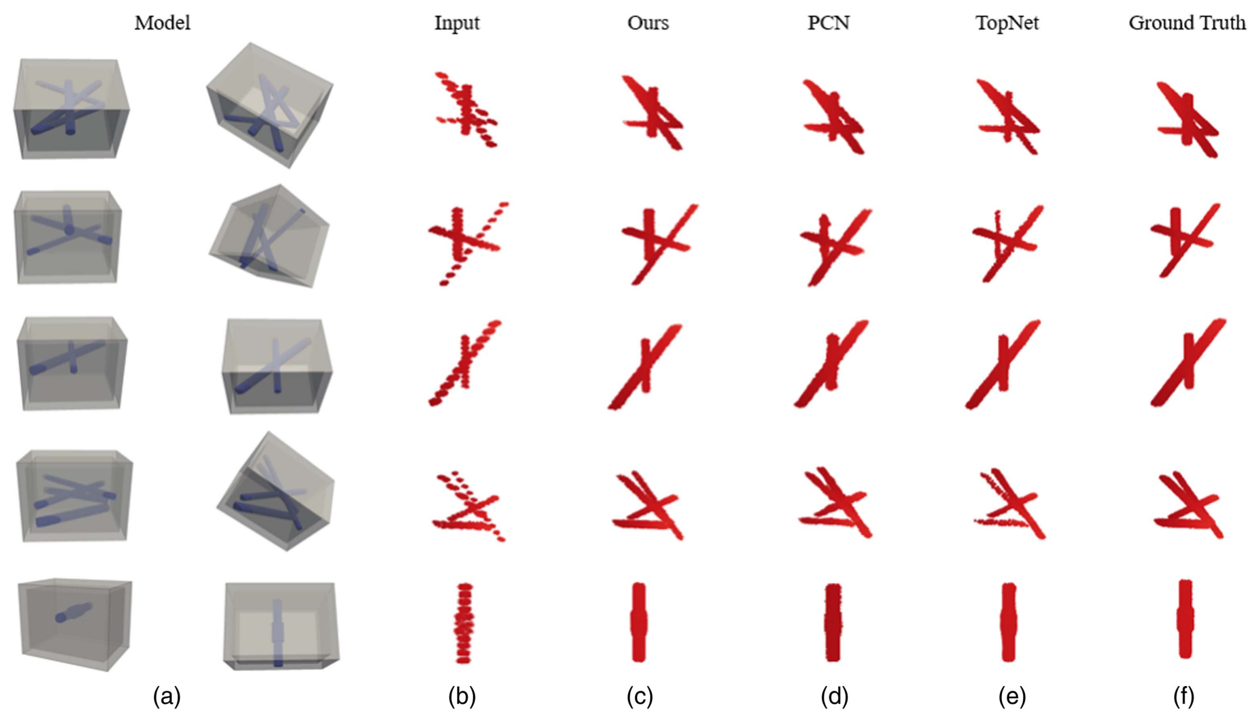

Fig. 14. Qualitative comparison results between GPRNet and baseline methods. The comparison of completion results between other methods and our network: (a) slab CAD model; (b) input data; (c) our method; (d) PCN; (e) TopNet; and (f) ground truth. The results show our method could reconstruct a better 3D model for visualization.

At last, Fig. 16(c) illustrates the reconstructed point cloud model using GPRNet, where the depth of the pipe is indicated. In field test, the positioning accuracy would affect the distribution of the sparse input, which would introduce the noise in reconstituted point cloud model. However, under the supervision learning of the ground truth, the model could cover the uneven distributed area and fill up with point clouds to reveal the real 3D model of the target. As we can see, compared with the traditional migration method, our method only requires a sparse input and further generate a fine and continuous output 3D model of underground pipes. It facilitates the GPR users to understand the complex raw GPR B-scan data.

In addition to the better performance, the data-collection time was also significantly reduced by using the proposed GPR-based robotic inspection platform. Without the robotic data-collection platform, the inspector has to push the GPR device to follow exactly premarked grid lines, bring the GPR device back to the start points, mark the scanned points, and take notes. Our robotic-based data-collection process would only take around 3 min to scan the outlined area shown in Fig. 16(a), whereas manual collection usually takes more than 15 min to cover the same area. We can conclude that our robotic-based data-collection system could provide a more efficient way for GPR-based construction surveys.

Table 8. Computational cost comparison among GPRNet, PCN, and TopNet

Method	Average time cost (ms)
GPRNet	8.04
PCN	8.62
TopNet	**7.91**

Note: Bold values indicate the better results.

Conclusion

This paper presented a robotic inspection system consisting of an omnidirectional robot and GPR postprocessing software to automate the GPR data-collection process and reconstruct a 3D model of underground utilities for construction surveys. Our omnidirectional robot allows the GPR device to move forward, backward, and sideways in a fast and swift manner. We proposed a low-cost solution for vision-based accurate positioning, localization, and mapping. By tagging the robot position information with GPR measurements at each sampling step in a synchronized way, it enables the robot to scan the surface in free-motion trajectory and facilitates high-resolution 3D GPR imaging. It eliminates the time, hassle, and cost of laying out grid lines on flat terrain and reduces the hassle to closely follow the grid lines and the note-taking time to record the linear motion trajectory in the X-Y directions in the current GPR data-collection process.

In addition, we proposed a DNN-based method for 3D GPR imaging that contains two modules: MigrationNet and GPRNet. We evaluated the performance and validated the feasibility of our innovative method in the experimental studies. By using synthetic data and real GPR data with a ground-truth value in our qualitative and quantitative experiments, it demonstrated that our 3D GPR imaging methods can produce a 3D model of underground utilities with less noisy data compared with the conventional BP-based migration. The concrete slab GPR data set is released to public and will benefit the research communities.

This study does have some limitations, which are as follows. One of the limitations lies in the limited amount of the real GPR data being used for training and testing the proposed methods. Although we have carefully designed the parameters of the GPR antenna in synthetic data generation, the real-world noise that exists in the real GPR data can hardly be simulated. Thus, we are also

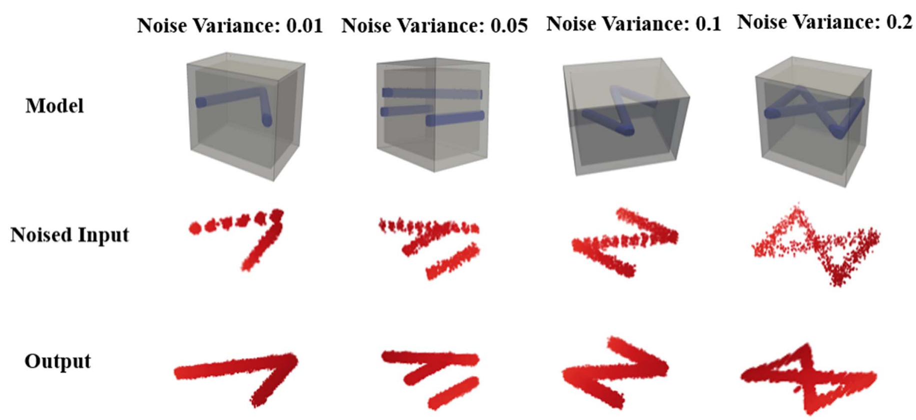

Fig. 15. Qualitative noise robustness results on GPRNet, which indicate the slab model, noise input with different noise variances, and the reconstructed point cloud model.

Table 9. Noise Robustness Evaluation between GPRNet and baselines with three metrics

	GPRNet			PCN			TopNet		
Metrics	CD	EMD	$\mathcal{L}_1$ distance	CD	EMD	$\mathcal{L}_1$ distance	CD	EMD	$\mathcal{L}_1$ distance
Variance and noise density = 0.01	**6.419**	**6.628**	**2.287**	6.901	7.266	2.619	6.894	7.024	2.5498
Variance and noise density = 0.05	**7.722**	**8.124**	**2.565**	7.965	8.313	2.702	8.248	8.480	2.7973
Variance and noise density = 0.1	**7.774**	**8.068**	**2.601**	8.141	8.458	2.783	8.489	8.517	2.857
Variance and noise density = 0.2	**8.069**	**8.369**	3.046	8.495	8.901	**2.956**	8.662	8.956	3.130

Note: Bold values indicate the better results.

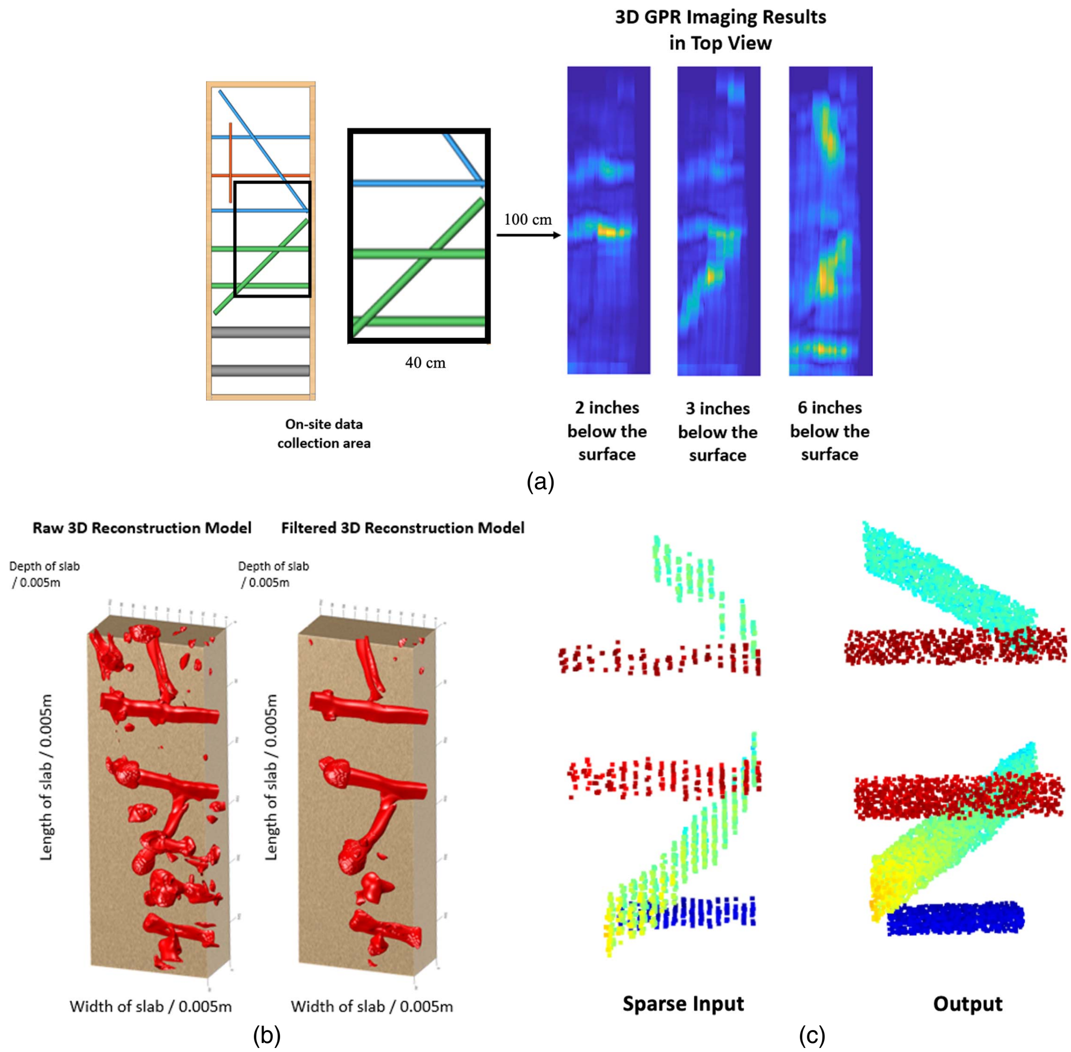

Fig. 16. GPR field 3D model results: (a) conventional migration 2D results for our collected field data at a concrete slab; (b) raw and filtered 3D model of the conventional migration result; and (c) reconstruction point cloud model using GPRNet.

consulting with field engineers to collect a large amount of field GPR data for training and testing to further increase our method's robustness. Another limitation of this article is that we only used GSSI PaveScan to test and verify the effectiveness of our proposed method. But we also believe our method is applicable to other GPR antenna models with different frequencies. We also plan to use other types of GPR antenna and design a more extensive robotic-based data-collection system in the near future.

Data Availability Statement

All GPR data and models are available for noncommercial use, and all the code that support the findings of this study are available from the corresponding author upon request.

Acknowledgments

Financial support for this study was provided by US National Science Foundation (NSF) Grant No. IIP-1915721, and by the US Department of Transportation under Grant No. 69A3551747126 through INSPIRE University Transportation Center at Missouri University of Science and Technology. The views, opinions, findings, and conclusions reflected in this publication are solely those of the authors and do not represent the official policy or position of the USDOT/OST-R, or any State or other entity. J Xiao has significant financial interest in InnovBot LLC, a company involved in R&D and commercialization of the technology.

Supplemental Materials

Videos S1 and S2 and Figs. S1–S3 are available online in the ASCE Library (www.ascelibrary.org).

References

Achlioptas, P., O. Diamanti, I. Mitliagkas, and L. Guibas. 2018. "Learning representations and generative models for 3D point clouds." In *Proc., Int. Conf. on Machine Learning*, 40–49. Cambridge, MA: Journal of Machine Learning Research.

Cai, J., P. Peng, H. Zeng, and S. Wang. 2020. "A cross correlation based back-projection imaging method for through-wall imaging." *J. Phys. Conf. Ser.* 1607 (1): 012020. https://doi.org/10.1088/1742-6596/1607/1/012020.

Campos, C., R. Elvira, J. J. G. Rodríguez, J. M. Montiel, and J. D. Tardós. 2021. "Orb-slam3: An accurate open-source library for visual, visual–inertial, and multimap slam." *IEEE Trans. Rob.* 37 (6): 1874–1890. https://doi.org/10.1109/TRO.2021.3075644.

Chetih, N., and Z. Messali. 2015. "Tomographic image reconstruction using filtered back projection (FBP) and algebraic reconstruction technique (ART)." In *Proc., 2015 3rd Int. Conf. on Control, Engineering & Information Technology (CEIT)*, 1–6. New York: IEEE.

Chou, C., A. Kingery, D. Wang, H. Li, and D. Song. 2018. "Encoder-camera-ground penetrating radar tri-sensor mapping for surface and subsurface transportation infrastructure inspection." In *Proc., 2018 IEEE Int. Conf. on Robotics and Automation (ICRA)*, 1452–1457. New York: IEEE.

Chou, C., H. Li, and D. Song. 2020. *Encoder-camera-ground penetrating radar sensor fusion: Bimodal calibration and subsurface mapping*. New York: IEEE.

Chou, C., S.-H. Yeh, and D. Song. 2017. "Mirror-assisted calibration of a multi-modal sensing array with a ground penetrating radar and a camera." In *Proc.,* 2017 IEEE/RSJ *Int. Conf. on Intelligent Robots and Systems (IROS)*, 1457–1463. New York: IEEE.

Chou, C., S.-H. Yeh, J. Yi, and D. Song. 2016. "Extrinsic calibration of a ground penetrating radar." In *Proc., 2016 IEEE Int. Conf. on Automation Science and Engineering (CASE)*, 1326–1331. New York: IEEE.

Claerbout, J. F., and S. M. Doherty. 1972. "Downward continuation of moveout-corrected seismograms." *Geophysics* 37 (5): 741–768. https://doi.org/10.1190/1.1440298.

Demirci, S., H. Cetinkaya, E. Yigit, C. Ozdemir, and A. A. Vertiy. 2012a. "A study on millimeter-wave imaging of concealed objects: Application using back-projection algorithm." *Prog. Electromagn. Res.* 128 (Jan): 457–477. https://doi.org/10.2528/PIER12050210.

Demirci, S., E. Yigit, I. H. Eskidemir, and C. Ozdemir. 2012b. "Ground penetrating radar imaging of water leaks from buried pipes based on back-projection method." *NDT&E Int.* 47 (Dec): 35–42. https://doi.org/10.1016/j.ndteint.2011.12.008.

Dinh, K., N. Gucunski, K. Tran, A. Novo, and T. Nguyen. 2021. "Full-resolution 3D imaging for concrete structures with dual-polarization GPR." *Autom. Constr.* 125 (May): 103652. https://doi.org/10.1016/j.autcon.2021.103652.

Fan, H., H. Su, and L. J. Guibas. 2017. "A point set generation network for 3D object reconstruction from a single image." In *Proc., IEEE Conf. on Computer Vision and Pattern Recognition*, 605–613. New York: IEEE.

Feng, J. 2022. "Public synthetic GPR dataset." Dropbox. Accessed September 22, 2022. https://www.dropbox.com/s/tv0ne4bgiql7nco/tgrs_models.tar.gz?dl=0.

Feng, J., L. Yang, E. Hoxha, D. Sanakov, S. Sotnikov, and J. Xiao. 2021a. "GPR-based model reconstruction system for underground utilities using GPRNET." In *Proc., 2021 IEEE Int. Conf. on Robotics and Automation (ICRA)*, 845–851. New York: IEEE.

Feng, J., L. Yang, E. Hoxha, and J. Xiao. 2022. "Improving 3D metric GPR imaging using automated data collection and learning-based processing." *IEEE Sens. J.* https://doi.org/10.1109/JSEN.2022.3164707.

Feng, J., L. Yang, H. Wang, Y. Tian, and J. Xiao. 2021b. "Subsurface pipes detection using DNN-based back projection on GPR data." In *Proc., IEEE/CVF Winter Conf. on Applications of Computer Vision*, 266–275. New York: IEEE.

Gazdag, J. 1978. "Wave equation migration with the phase-shift method." *Geophysics* 43 (7): 1342–1351. https://doi.org/10.1190/1.1440899.

Gharamohammadi, A., F. Behnia, and A. Shokouhmand. 2019. "Imaging based on a fast back-projection algorithm considering antenna beamwidth." In *Proc., 2019 6th Iranian Conf. on Radar and Surveillance Systems*, 1–4. New York: IEEE.

Giannakis, I., A. Giannopoulos, and C. Warren. 2018. "Realistic FDTD GPR antenna models optimized using a novel linear/nonlinear full-waveform inversion." *IEEE Trans. Geosci. Remote Sens.* 57 (3): 1768–1778. https://doi.org/10.1109/TGRS.2018.2869027.

Godard, C., O. Mac Aodha, and G. J. Brostow. 2017. "Unsupervised monocular depth estimation with left-right consistency." In *Proc., IEEE Conf. on Computer Vision and Pattern Recognition*, 270–279. New York: IEEE.

González-Huici, M. A., I. Catapano, and F. Soldovieri. 2014. "A comparative study of GPR reconstruction approaches for landmine detection." *IEEE J. Sel. Top. Appl. Earth Obs. Remote Sens.* 7 (12): 4869–4878. https://doi.org/10.1109/JSTARS.2014.2321276.

Hou, F., W. Lei, S. Li, J. Xi, M. Xu, and J. Luo. 2021. "Improved mask R-CNN with distance guided intersection over union for GPR signature detection and segmentation." *Autom. Constr.* 121 (Jan): 103414. https://doi.org/10.1016/j.autcon.2020.103414.

Huang, Z., Y. Yu, J. Xu, F. Ni, and X. Le. 2020. "PF-Net: Point fractal network for 3D point cloud completion." In *Proc., IEEE/CVF Conf. on Computer Vision and Pattern Recognition*, 7662–7670. New York: IEEE.

Jacobsen, S., and Y. Birkelund. 2010. "Improved resolution and reduced clutter in ultra-wideband microwave imaging using cross-correlated back projection: Experimental and numerical results." *J. Biomed. Imaging* 2010 (1): 20. https://doi.org/10.1155/2010/781095.

Li, H., C. Chou, L. Fan, B. Li, D. Wang, and D. Song. 2018. "Robotic subsurface pipeline mapping with a ground-penetrating radar and a camera." In *Proc.,* 2018 IEEE/RSJ *Int. Conf. on Intelligent Robots and Systems (IROS)*, 3145–3150. New York: IEEE.

Li, H., C. Chou, L. Fan, B. Li, D. Wang, and D. Song. 2019. "Toward automatic subsurface pipeline mapping by fusing a ground-penetrating radar and a camera." *IEEE Trans. Autom. Sci. Eng.* 17 (2): 722–734. https://doi.org/10.1109/TASE.2019.2941848.

Li, S., H. Cai, D. M. Abraham, and P. Mao. 2016a. "Estimating features of underground utilities: Hybrid GPR/GPS approach." *J. Comput. Civ. Eng.* 30 (1): 04014108. https://doi.org/10.1061/(ASCE)CP.1943-5487.0000443.

Li, S., C. Yuan, D. Liu, and H. Cai. 2016b. "Integrated processing of image and GPR data for automated pothole detection." *J. Comput. Civ. Eng.* 30 (6): 04016015. https://doi.org/10.1061/(ASCE)CP.1943-5487.0000582.

Lin, C., X. Wang, Y. Li, F. Zhang, Z. Xu, and Y. Du. 2020. "Forward modelling and GPR imaging in leakage detection and grouting evaluation in tunnel lining." *KSCE J. Civ. Eng.* 24 (1): 278–294. https://doi.org/10.1007/s12205-020-1530-z.

Lin, T.-Y., P. Dollár, R. Girshick, K. He, B. Hariharan, and S. Belongie. 2017. "Feature pyramid networks for object detection." In *Proc., IEEE Conf. on Computer Vision and Pattern Recognition*, 2117–2125. New York: IEEE.

Liu, H., Z. Chen, H. Lu, F. Han, C. Liu, J. Li, and J. Cui. 2020. "Migration of ground penetrating radar with antenna radiation pattern correction." *IEEE Geosci. Remote Sens. Lett.* 19 (7): 1–5. https://doi.org/10.1109/LGRS.2020.3026207.

Merriaux, P., Y. Dupuis, R. Boutteau, P. Vasseur, and X. Savatier. 2017. "A study of vicon system positioning performance." *Sensors* 17 (7): 1591. https://doi.org/10.3390/s17071591.

Pereira, M., D. Burns, D. Orfeo, R. Farrel, D. Hutson, and T. Xia. 2018a. "New GPR system integration with augmented reality based positioning." In *Proc., 2018 on Great Lakes Symp. on VLSI*, 341–346. New York: Association for Computing Machinery.

Pereira, M., D. Burns, D. Orfeo, Y. Zhang, L. Jiao, D. Huston, and T. Xia. 2020. *3-D multistatic ground penetrating radar imaging for augmented reality visualization*. New York: IEEE.

Pereira, M., Y. Zhang, D. Huston, and T. Xia. 2019a. "3-D SAR imaging for multistatic GPR." In *Image sensing technologies: Materials, devices, systems, and applications VI*. Bellingham, WA: International Society for Optics and Photonics.

Pereira, M., Y. Zhang, D. Orfeo, D. Burns, D. Huston, and T. Xia. 2018b. "3D tomography for multistatic GPR subsurface sensing." In *Radar sensor technology XXII*. Bellingham, WA: International Society for Optics and Photonics.

Pereira, M., Y. Zhang, D. Orfeo, D. Burns, D. Huston, and T. Xia. 2019b. "3D tomographic image reconstruction for multistatic ground penetrating radar." In *Proc., 2019 IEEE Radar Conf. (RadarConf)*, 1–6. New York: IEEE.

Qi, C. R., H. Su, K. Mo, and L. J. Guibas. 2017a. "Pointnet: Deep learning on point sets for 3D classification and segmentation." In *Proc., IEEE Conf. on Computer Vision and Pattern Recognition*, 652–660. New York: IEEE.

Qi, C. R., L. Yi, H. Su, and L. J. Guibas. 2017b. "Pointnet++: Deep hierarchical feature learning on point sets in a metric space." *Adv. Neural Inf. Process. Syst.* 30 (1): 5099–5108.

Qin, H., D. Zhang, Y. Tang, and Y. Wang. 2021. "Automatic recognition of tunnel lining elements from GPR images using deep convolutional networks with data augmentation." *Autom. Constr.* 130 (Jan): 103830. https://doi.org/10.1016/j.autcon.2021.103830.

Ronneberger, O., P. Fischer, and T. Brox. 2015. "U-net: Convolutional networks for biomedical image segmentation." In *Proc., Int. Conf. on Medical Image Computing and Computer-Assisted Intervention*, 234–241. Berlin: Springer.

Schneider, W. A. 1978. "Integral formulation for migration in two and three dimensions." *Geophysics* 43 (1): 49–76. https://doi.org/10.1190/1.1440828.

Schofield, R., L. King, U. Tayal, I. Castellano, J. Stirrup, F. Pontana, J. Earls, and E. Nicol. 2020. "Image reconstruction: Part 1—Understanding filtered back projection, noise and image acquisition." *J. Cardiovasc. Comput. Tomogr.* 14 (3): 219–225. https://doi.org/10.1016/j.jcct.2019.04.008.

Stadler, S., and J. Igel. 2018. "A numerical study on using guided GPR waves along metallic cylinders in boreholes for permittivity sounding." In *Proc., 2018 17th Int. Conf. on Ground Penetrating Radar (GPR)*, 1–4. New York: IEEE.

Tchapmi, L. P., V. Kosaraju, H. Rezatofighi, I. Reid, and S. Savarese. 2019. "Topnet: Structural point cloud decoder." In *Proc., IEEE Conf. on Computer Vision and Pattern Recognition*, 383–392. New York: IEEE.

Wang, Z., A. C. Bovik, H. R. Sheikh, and E. P. Simoncelli. 2004. "Image quality assessment: From error visibility to structural similarity." *IEEE Trans. Image Process.* 13 (4): 600–612. https://doi.org/10.1109/TIP.2003.819861.

Warren, C., and A. Giannopoulos. 2011. "Creating finite-difference time-domain models of commercial ground-penetrating radar antennas using Taguchi's optimization method." *Geophysics* 76 (2): G37–G47. https://doi.org/10.1190/1.3548506.

Warren, C., A. Giannopoulos, and I. Giannakis. 2016. "GPRMax: Open source software to simulate electromagnetic wave propagation for ground penetrating radar." *Comput. Phys. Commun.* 209 (Aug): 163–170. https://doi.org/10.1016/j.cpc.2016.08.020.

Wells, D., et al. 1987. *Guide to GPS positioning*. Berlin: Citeseer.

Xiang, Z., G. Ou, and A. Rashidi. 2021. "Robust cascaded frequency filters to recognize rebar in GPR data with complex signal interference." *Autom. Constr.* 124 (Apr): 103593. https://doi.org/10.1016/j.autcon.2021.103593.

Xie, X., J. Zhai, and B. Zhou. 2020. "Back-fill grouting quality evaluation of the shield tunnel using ground penetrating radar with bi-frequency back projection method." *Autom. Constr.* 121 (Jan): 103435. https://doi.org/10.1016/j.autcon.2020.103435.

Yang, Y., C. Feng, Y. Shen, and D. Tian. 2018. "Foldingnet: Point cloud auto-encoder via deep grid deformation." In *Proc., IEEE Conf. on Computer Vision and Pattern Recognition*, 206–215. New York: IEEE.

Yuan, C., S. Li, H. Cai, and V. R. Kamat. 2018a. "GPR signature detection and decomposition for mapping buried utilities with complex spatial configuration." *J. Comput. Civ. Eng.* 32 (4): 04018026. https://doi.org/10.1061/(ASCE)CP.1943-5487.0000764.

Yuan, W., T. Khot, D. Held, C. Mertz, and M. Hebert. 2018b. "PCN: Point completion network." In *Proc., 2018 Int. Conf. on 3D Vision (3DV)*, 728–737. New York: IEEE.

Zhang, H., O. Shan, G. Wang, J. Li, S. Wu, and F. Zhang. 2015. "Back-projection algorithm based on self-correlation for ground-penetrating radar imaging." *J. Appl. Remote Sens.* 9 (1): 095059. https://doi.org/10.1117/1.JRS.9.095059.

Zhao, H., O. Gallo, I. Frosio, and J. Kautz. 2015. "Loss functions for neural networks for image processing." Preprint, submitted November 28, 2015. https://doi.org/10.48550/arXiv.1511.08861.

Zhou, L., C. Huang, and Y. Su. 2011. "A fast back-projection algorithm based on cross correlation for GPR imaging." *IEEE Geosci. Remote Sens. Lett.* 9 (2): 228–232. https://doi.org/10.1109/LGRS.2011.2165523.